Science of the Total Environment 575 (2017) 612–627

Contents lists available at ScienceDirect

Science of the Total Environment

journal homepage: www.elsevier.com/locate/scitotenv

Optical and radiative properties of aerosols over Desalpar, a remote site in western India: Source identification, modification processes and aerosol type discrimination

Piyushkumar N. Patel [a], U.C. Dumka [b,*], D.G. Kaskaoutis [c], K.N. Babu [a], Alok K. Mathur [a]

[a] Calibration & Validation Division, Space Applications Centre, ISRO, Ahmedabad 380 015, India.
[b] Aryabhatta Research Institute of Observational Sciences, Nainital 263 001, India
[c] Atmospheric Research Team, Institute for Environmental Research and Sustainable Development, National Observatory of Athens, GR, 11810 Athens, Greece

HIGHLIGHTS

- Aerosol characterization carried out for the first time over Desalpar, a semi-arid site in western India.
- The aerosol optical properties exhibit important seasonality.
- Dominance of mixed-type aerosols with significant contribution of marine-influenced particles.
- Increase in direct radiative forcing and atmospheric heating rate due to dust advection.

GRAPHICAL ABSTRACT

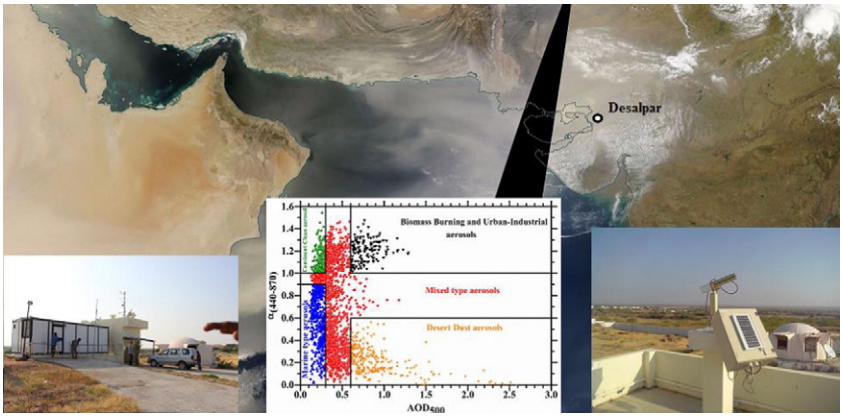

ARTICLE INFO

Article history:
Received 5 August 2016
Received in revised form 1 September 2016
Accepted 4 September 2016
Available online 8 September 2016

Editor: D. Barcelo

Keywords:
Aerosol physical-optical properties
Aerosol types
Radiative forcing
Sector influence
Western India

ABSTRACT

Aerosol optical properties are analyzed for the first time over Desalpar (23.74°N, 70.69°E, 30 m above mean sea level) a remote site in western India during October 2014 to August 2015. Spectral aerosol optical depth (AOD) measurements were performed using the CIMEL CE-318 automatic Sun/sky radiometer. The annual-averaged AOD_{500} and Ångström exponent ($\alpha_{440-870}$) values are found to be 0.43 ± 0.26 and 0.69 ± 0.39, respectively. On the seasonal basis, high AOD_{500} of 0.45 ± 0.30 and 0.61 ± 0.34 along with low $\alpha_{440-870}$ of 0.41 ± 0.27 and 0.41 ± 0.35 during spring (March–May) and summer (June–August), respectively, suggest the dominance of coarse-mode aerosols, while significant contribution from anthropogenic sources is observed in autumn (AOD_{500} = 0.47 ± 0.26, $\alpha_{440-870}$ = 1.02 ± 0.27). The volume size distribution and the spectral single-scattering albedo also confirm the presence of coarse-mode aerosols during March–August. An overall dominance of a mixed type of aerosols (~56%) mostly from October to February is found via the AOD_{500} vs $\alpha_{440-870}$ relationship, while marine aerosols contribute to ~18%. Spectral dependence of α and its second derivative (α′) are also used for studying the aerosol modification processes. The average direct aerosol radiative forcing (DARF) computed via the SBDART model is estimated to range from −27.08 W m^{-2} to −10.74 W m^{-2} at the top of the atmosphere, from −52.21 W m^{-2} to −21.71 W m^{-2} at the surface and from 10.97 W m^{-2} to 26.54 W m^{-2} within

* Corresponding author at: ARIES, Manora Peak, Nainital 263 001, Uttarakhand, India.
E-mail addresses: dumka@aries.res.in, ucdumka@gmail.com (U.C. Dumka).

http://dx.doi.org/10.1016/j.scitotenv.2016.09.023

the atmosphere. This atmospheric forcing translates into heating rates of 0.31–0.75 K day^{-1}. The aerosol properties and DARF are also examined for different trajectory clusters in order to identify the sources and to assess the influence of long-range transported aerosols over Desalpar.

1. Introduction

Atmospheric aerosols (natural and anthropogenic) are one of the most important constituents in the Earth-atmosphere system (IPCC, 2013). Aerosols play a crucial role in influencing the Earth radiation budget and local/regional climate specifically in south Asia by interacting with incoming solar and outgoing terrestrial radiation and clouds through the direct and indirect effects. They also affect the monsoon circulation, hydrological cycle and melting of the Himalayan glaciers and snow packs (Hansen et al., 2000; Ramanathan et al., 2001; Bollasina et al., 2008; Gautam et al., 2010; Bond et al., 2013). On the other hand, aerosols constitute one of the largest sources of uncertainty in the estimation of present climate forcing due to their large spatial-temporal heterogeneity and short residence time in the atmosphere (Satheesh and Moorthy, 2005; Lawrence and Lelieveld, 2010; and references therein). The rapid economic development and increasing energy demands have been drastically increasing the aerosol emissions and loading over Asia, especially in India and China (e.g. Lu et al., 2010; Lawrence, 2011; Yoon et al., 2011, 2012, 2014; Saikawa et al., 2011; Babu et al., 2013; Moorthy et al., 2013; Cui et al., 2015; Wang et al., 2016). More specifically, Chin et al. (2003) found that intensive forest and agricultural fires and desertification over specific regions in East Asia contribute around 25%–33% to the global emissions of different aerosol types (e.g. SO_2, organic matter, black carbon and dust).

Aerosol studies over the Indian sub-continent have been mostly focusing on examining the aerosol loading, properties, types, source regions and climate implications over the densely populated and severe-polluted Indo-Gangetic Plains (IGP) (e.g., Singh et al., 2004; Ram et al., 2010; Kaskaoutis et al., 2013, 2014; Srivastava and Ramachandran, 2013; Dumka et al., 2014; Kedia et al., 2014; Das et al., 2015; and references therein). Several studies over sites in the IGP examined the influence of dust plumes originating mostly from the Thar Desert and southwest Asia on aerosol characteristics and radiative forcing (Dey et al., 2004; Prasad and Singh, 2007; Prasad et al., 2007; Sharma et al., 2012; Srivastava et al., 2014a; Alam et al., 2014; Kumar et al., 2015a; and references therein), but few studies refer to sites close or within the Thar Desert (Moorthy et al., 2007). Especially over the western part of India bordering Pakistan, to which the current location (i.e. Desalpar) belongs (see Fig. 1), the aerosol studies were mostly carried out over the urban/industrial area of Ahmedabad (Ganguly and Jayaraman, 2006; Ganguly et al., 2006a; Raman and Ramachandran, 2010; Ramachandran and Kedia, 2010). Furthermore, aerosol properties have been examined over an urban semi-arid site (Udaipur) and a hill-top station representing background conditions (Mt. Abu) located north of Desalpar (Das and Jayaraman, 2011). The megacity Karachi is located about 400 km west from Desalpar, where important studies on aerosol properties have been performed (Alam et al., 2011, 2012).

The present work focuses on examining the column-integrated aerosol optical, physical and radiative properties for the first time at Desalpar, located between the southern tips of the Thar Desert and Indus river delta, close to the north-easternmost edge of the Arabian Sea (see Fig. 1). The analysis utilizes eleven months (October 2014 to August 2015) of high-quality level 2 data of aerosol optical and physical properties derived from Sun-photometer (CIMEL CE-318). The main objectives of the current work are to study (i) the temporal (diurnal, daily, seasonal) variability of the aerosol properties, (ii) the dominant aerosol types based on correlations between aerosol optical depth (AOD) and Ångström exponent (α), (iii) the aerosol modification processes in the

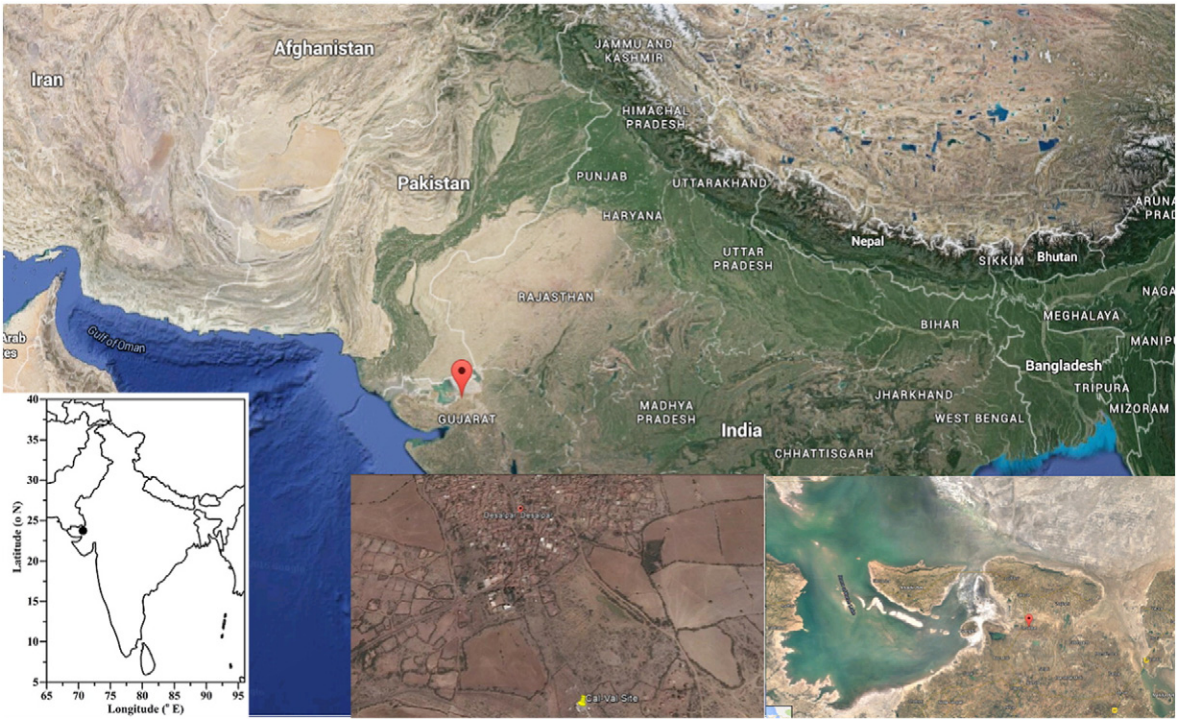

Fig. 1. Geographical location of Desalpar (DES) over Indian subcontinent.

atmosphere, (iv) the aerosol transport pathways and source identification via the Hybrid Single Particle Lagrangian Integrated Trajectory (HYSPLIT) model and, (v) the direct aerosol radiative forcing (DARF) and atmospheric heating rates (HR) by means of the Santa Barbara DISORT Atmospheric Radiative Transfer (SBDART) model. Although the current work covers eleven months of preliminary aerosol observations, the findings may be helpful for the aerosol science in India since the measuring site is in the crossroad of seasonally-changing air masses coming from the Thar Desert, Indus Valley, Arabian Sea and southwest Asia.

2. Materials and methods

2.1. Site description and measurements

The observational site (Desalpar; 23.74°N, 70.69°E, 30 m above mean sea level) is a remote village located in the western part of India close to the Pakistan borders. The site is located in an area between the southern tips of the Thar Desert and Indus Valley, while it opens to the Gulf of Kutch and the Arabian Sea in the southwest (Fig. 1). The site is influenced by dust aerosols emitted from the Thar Desert, anthropogenic aerosols from the densely populated Indus Valley and marine particles from the Arabian Sea. Furthermore, under certain circumstances the site is in the downwind direction of intense dust storms originated from Arabia and transported across the northern Arabian Sea to India (Jish Prakash et al., 2014; Srivastava et al., 2014a) or even severe dust storms originated from the Sistan Basin in Iran (Alam et al., 2011; Rashki et al., 2015). The great Rann Kutch Lake lies to the west of the measuring site, which has salty clay and is prone to significant changes due to evaporation, while few power plants exist towards southwest. Desalpar is dominated by a steppe/arid climate and low of rainfall throughout the year. The average annual temperature is ~26°C with a total rainfall of 398 mm (source: http://en.climate-data.org/location/693972/).

As a part of the calibration and validation program (Shukla et al., 2013), measurements of columnar aerosol properties were carried out over Desalpar using the ground-based automatic CIMEL CE-318 Sun/sky radiometer. The period from October 2014 to August 2015 is analyzed in the current study, since during September–November 2015, the instrument stopped its operation and was sent for calibration. The radiometer measures both direct Sun irradiance and diffuse sky radiances in the spectral range 340–1020 nm and 440–1020 nm, respectively with a field of view of 1.2°. More specifically, the direct solar irradiance is measured at eight wavelengths centered at 340, 380, 440, 500, 675, 870, 940 and 1020 nm. The measurements at 940 nm are used for the estimation of columnar precipitable water vapor content (WVC) and the remaining wavelengths are used for the estimation of spectral AOD. All the filters used in the CIMEL CE-318 radiometer are narrowband with a bandwidth of 10 nm except for 340 nm and 380 nm with a bandwidth of 2 nm. On the other hand, sky almucantar radiances from principal plane measurements were performed at 440, 675, 870 and 1020 nm for retrievals of the optical and microphysical properties of aerosols such as single scattering albedo (SSA), volume size distribution (VSD), asymmetry parameter and refractive index. The standard protocol for direct-Sun measurements is a triplet of observations every 15 min, while the sky-almucantar measurements were performed every 30 min. The high-quality Level 2 data were used in the current study and averaged on daily, monthly and seasonal (autumn: October–November; winter: December–February; spring: March–May and summer: June–August) basis. During the measuring period, Sun/sky radiometer measurements were performed on 271 days corresponding to 2632 hourly data, as summarized in the Supplementary Table S-1. Further details about the instrument characteristics and aerosol retrievals are given elsewhere (Estellés et al., 2012). In contrast to the AERONET and SKYNET inversion algorithms, we used a new open source package (ESR.pack; Estellés et al., 2012), which is basically based on the Skyrad.pack (version 4.2) algorithm used in SKYNET (Nakajima et al., 1996a). The ESR.pack has been modified and adapted for application to CIMEL CE-318 Sun/sky radiometer and consists of two basic modules i) Sunrad for the retrieval of direct Sun products (e.g. AOD, α, and WVC) and ii) Skyrad, which is a modified version of Skyrad.pack v4.2 (Nakajima et al., 1996b; Kobayashi et al., 2010), to invert the sky radiance for the estimation of VSD, SSA, asymmetry parameter and refractive index. More details about the ESR algorithm, methodology, uncertainties, calibration and inter-comparison with AERONET and SKYNET are presented elsewhere (Campanelli et al., 2004, 2007; Estellés et al., 2012; and references therein). Although AOD, α and WVC are retrieved for each scan under clear-sky conditions, the inversion products are given on daily-mean basis.

2.2. Ångström exponent and its derivatives

The spectral dependence of AOD is well represented by the Ångström power law ($\tau_\lambda = \beta\lambda^{-\alpha}$), where λ is the wavelength in μm, α is the Ångström wavelength exponent and β is the turbidity coefficient, which equals to AOD at $\lambda = 1$ μm. α gives useful information about the aerosol size and fine-to-coarse mode fraction; higher values of α indicate the dominance of fine-mode aerosols, whereas α close to zero corresponds to coarse-mode aerosols such as dust and sea salt (Eck et al., 2005). In the present study, α was estimated via the Volz method following Eq. (1) in three wavelength ranges i.e., 440–870 nm, 440–675 nm and 675–870 nm:

$$\alpha = -\frac{\ln\left(\frac{\tau_{\lambda 1}}{\tau_{\lambda 2}}\right)}{\ln\left(\frac{\lambda_1}{\lambda_2}\right)} \quad (1)$$

where, $\tau_{\lambda 1}$ and $\tau_{\lambda 2}$ represent the AOD at two wavelengths λ_1 and λ_2. Generally, the aerosol size distribution contains both fine and coarse-mode particles of different origin and characteristics and departs from the Junge power-law (Eck et al., 1999, 2005). This leads the lnAOD vs lnλ curve to deviate from linearity and to be simulated better by a second-order polynomial fit as:

$$\ln\tau_\lambda = a_2(\ln\lambda)^2 + a_1(\ln\lambda) + a_0 \quad (2)$$

where a_0, a_1 and a_2 are constants that can be obtained from the Sun/sky radiometer measurements. The coefficient a_2 represents the curvature, which can be either negative or positive indicating that the size distribution is dominated by fine- or coarse-mode aerosols, respectively (Eck et al., 1999; Schuster et al., 2006; Kaskaoutis et al., 2007). The curvature can be estimated by the first and second derivatives of Eq. ((2) with respect to lnλ as:

$$\frac{d\ln\tau}{d\ln\lambda} = 2\,a_2\ln\lambda + a_1 \quad (3)$$

and

$$\frac{d^2\ln\tau}{d(\ln\lambda)^2} = -\frac{d\alpha}{d\ln\lambda} = 2a_2 \quad (4)$$

taking also into account the Eq. (1). Therefore, the second derivative of AOD with respect to lnλ provides the derivative of α (α′) that equals to $-2a_2$:

$$\alpha' = \frac{d\alpha}{d\ln\lambda} = -2a_2 \quad (5)$$

Positive values of α` indicate abundance of fine-mode particles in the size distribution whereas near zero or negative values of α′ show higher amount of coarse-mode aerosols (Eck et al., 2005).

2.3. Aerosol inversion products

Besides spectral AOD, α and its spectral dependence, an inversion algorithm can provide valuable information combining the direct Sun and diffuse sky-radiance measurements. The column-integrated aerosol VSD (dV(r) / dlnr) is one of the crucial parameters for understanding the aerosol scattering processes and radiative impact (Sinha et al., 2013). VSD has been estimated at 22 radius bins ranging from 0.05 to 10 μm and exhibits a bimodal distribution simulated by two log-normal distributions as:

$$\frac{dV(r)}{d\ln r} = \sum_{i=1}^{2} \frac{C_{v,\ i}}{\sqrt{2\pi}\sigma_i} \exp\left[\frac{(\ln r - \ln r_{v,\ i})^2}{2\sigma_i^2}\right] \quad (6)$$

where the r_{vi}, σ_i, and C_{vi} are the volume mean radius, the geometric standard deviation, and the volume concentration of fine and coarse mode aerosols, respectively. In addition to VSD, the inversion algorithms provide the spectral SSA at four wavelengths (440, 675, 870, 1020 nm), which is an important parameter for the estimation of DARF. Furthermore, retrievals of the asymmetry parameter, real and imaginary parts of the refractive index have been performed and their seasonal variations are presented in the Supplementary material (Suppl. Figs. S-1 and S-2).

2.4. Estimation of DARF and atmospheric heating rate

DARF at the top of the atmosphere (TOA) and surface (SFC) is defined as the net change in radiative flux caused by atmospheric aerosols as:

$$\Delta F_{TOA,SFC} = (\text{Net Flux})_{\text{With aerosol}_{TOA,SFC}} - (\text{Net Flux})_{\text{Without aerosol}_{TOA,SFC}} \quad (7)$$

The difference between ARF at TOA and SFC is defined as the net atmospheric forcing (ATM), which represents the amount of solar radiation absorbed by aerosols within the atmosphere ($\Delta F_{ATM} = \Delta F_{TOA} - \Delta F_{SFC}$). The clear-sky DARF was estimated in the short-wavelength region (0.25–4.0 μm) at SFC, TOA and ATM using the Sun/sky radiometer measurements of spectral values of AOD, SSA, and asymmetry factor as the fundamental input parameters into the SBDART model (Ricchiazzi et al., 1998). In addition to the aerosol optical properties, the vertical profiles of atmospheric parameters (i.e., temperature, relative humidity, pressure, water vapor and ozone), the WVC and the surface reflectance at the observational site are crucial parameters in the SBDART. In the present study, the tropical atmospheric profiles and the MODIS (both Terra and Aqua) surface albedo (8-day, Level 3, Global 500 m SIN Grid product) at seven wavelengths (0.645, 0.859, 0.469, 0.555, 1.24, 1.64 and 2.13 μm) were used as inputs to SBDART. DARF was estimated using eight radiation streams in order to obtain the TOA and SFC downward and upward fluxes at every one-hour interval for a 24-hour period with and without aerosols and the diurnally-averaged radiative forcing at TOA and SFC was then obtained as the difference between net fluxes (down-up) with and without aerosols. Further details of the use of MODIS surface albedo, DARF estimations and uncertainties are presented elsewhere (Dumka et al., 2014; Srivastava et al., 2014b; Bisht et al., 2015). The atmospheric heating rate (HR) due to the absorption of solar radiation by aerosols in the atmosphere (net atmospheric forcing ΔF_{ATM}) was estimated from the first law of thermodynamics and hydrostatic equilibrium (Liou, 2002) as:

$$\frac{\partial T}{\partial t} = \frac{g}{C_P} \times \frac{\Delta F_{ATM}}{\Delta P} \times 24\left({}^{h}/_{day}\right) \times 3600\left({}^{s}/_{h}\right) \quad (8)$$

where $\partial T/\partial t$ is the heating rate in K day^{-1}, g/C_p is the lapse rate, g is the acceleration due to gravity and C_p the specific heat capacity of the air at constant pressure (1006 J kg^{-1} K^{-1}); ΔP is the atmospheric pressure difference for the layer in which most of the aerosols occur and is taken as 300 hPa similarly to previous studies (e.g., Dumka et al., 2014; Bisht et al., 2015).

2.5. Transport pathways

In order to examine the long-range transport pathways and source identification of aerosol types and properties, five-days isentropic air mass back-trajectories ending at 500 m, 1000 m and 4000 m agl over Desalpar were obtained from the HYSPLIT model (Draxler and Rolph, 2016) for individual days of Sun-photometer measurements. The meteorological data from NCEP/NCAR re-analysis were used in the trajectory simulations. Considering the main trajectory advection paths over Desalpar, four geographical sectors for boundary layer (500 m and 1000 m) and two for free-troposphere (4000 m) were identified using the cluster analysis technique (Dumka et al., 2010, 2013; Bisht et al., 2015). Although an air-mass back trajectory at a particular altitude may not accurately represent the dominant aerosol type because the trajectory sectors might be different at various altitudes, the aerosol characteristics and DARF values are examined for the trajectory clusters. The main sectors for back-trajectory pathways over Desalpar were found to be:

1. The southwestern sector associated with air-masses coming from the southwestern Arabian Sea and the tropical Indian Ocean associated with the summer monsoon circulation. These air masses are expected to carry marine aerosols over the measuring site mixed with dust coming from Arabia and southwest Asia and are dominant during the summer season (Kaskaoutis et al., 2010).
2. The western sector, which is associated with either air masses traveling very long distances from the Sahara desert and the Middle East mostly at 4000 m or air masses originating from Arabia and arid regions in Iran and Pakistan rich in Desert-dust aerosols. The air masses travelling at 4000 m or even above do not affect significantly the aerosol properties over Desalpar, since they have lost a main part of the aerosol loading during their long-range transport.
3. The local sector, which is associated with aerosols from nearby sources i.e., Thar Desert, Indus Valley and pollution plumes from urban/industrialized centers like Ahmedabad and Karachi (Ganguly and Jayaraman, 2006; Ganguly et al., 2006a; Alam et al., 2011).

3. Results and discussion

3.1. Temporal variation of aerosols

AOD is representative of the aerosol loading in the atmospheric column, while α gives useful information for the aerosol size and constitutes an important parameter for aerosol-type identification. The temporal variability of the daily-averaged AOD at 500 nm (AOD_{500}) values during the study period (October 2014 to August 2015) is shown in Fig. 2, while $\alpha_{440-870}$ is visualized by means of a color scale. The daily-averaged AOD_{500} ranges from ~0.13, corresponding to clean-background conditions over Desalpar, up to ~1.5 or even ~2.3 in certain cases due to the influence of dust storms, as those cases are associated with very low (<0.16) $\alpha_{440-870}$ values. The high variability in both AOD_{500} and $\alpha_{440-870}$ indicates a variety of aerosol types over the region due to transported air masses of different origin and characteristics. There is a clear differentiation between the high and low α values since the high values (bluish color) are found during the October–February period (fine-mode aerosols), while the low $\alpha_{440-870}$ (reddish color) are shown from March to August (coarse-mode aerosols). Fig. 2 also reveals that the larger day-to-day variability in both AOD_{500} and $\alpha_{440-870}$ exists from March to August, indicating significant changes in air-mass origin and characteristics, while the much lower variability from November to February indicates more stable atmospheric conditions and aerosol characteristics. However, cases associated with high AOD_{500} and $\alpha_{440-870}$ may also exist during late-autumn and winter

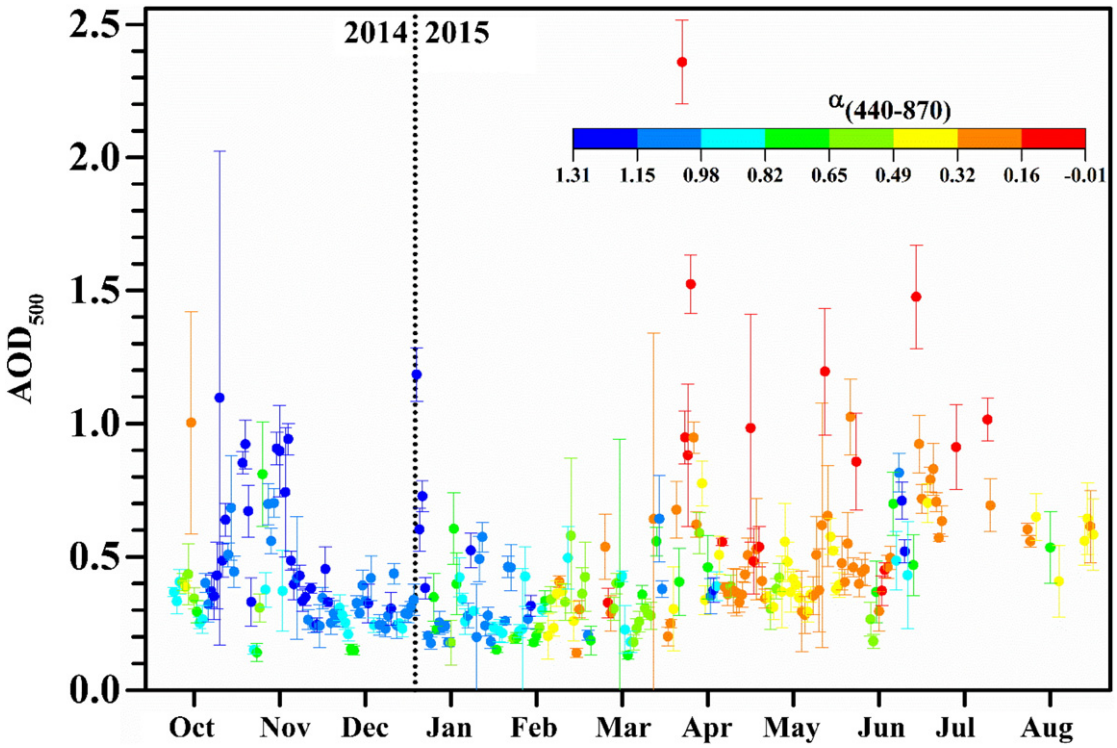

Fig. 2. Daily-mean variation of AOD_{500} over Desalpar in the period October 2014–August 2015. $\alpha_{440-870}$ is visualized by means of a color scale. The vertical bars correspond to one standard deviation from the daily AOD_{500} means.

corresponding to transported biomass burning and anthropogenic pollution plumes (Ganguly et al., 2006a; Kaskaoutis et al., 2014). During the whole period, the mean values of AOD_{500} and $\alpha_{440-870}$ were found to be 0.43 ± 0.26 and 0.69 ± 0.39, respectively.

Fig. 3, shows the monthly variation of AOD values at three wavelengths (340, 500 and 1020 nm), WVC and α values at three wavelength bands (440–870 nm, 440–675 nm, and 675–870 nm) in Box–Whisker plots. Examining the α values at various bands in the short- and long-wavelengths gives useful information about changes in the fine-mode radii and fine-mode fraction, respectively, while the difference in α values between short and long wavelengths define the sign and magnitude of the curvature in Eq. ((2) (Eck et al., 1999; Schuster et al., 2006). The AOD monthly variation (Fig. 3a) shows a distinct annual pattern with a decreasing tendency from autumn to winter and then a continuous increase during the spring and summer months attaining a maximum in July. The AOD annual pattern over Desalpar exhibits great similarities with that observed over the Arabian Sea (Kaskaoutis et al., 2011a). As expected, AOD_{340} is larger in all months compared to AOD_{500} and AOD_{1020}, while the range in AOD values at the specified wavelengths changes significantly from month-to-month indicating more or less homogeneity in the aerosol loading within a month. On seasonal basis, AOD_{500} was found to be 0.61 ± 0.34, 0.47 ± 0.26, 0.45 ± 0.30 and 0.31 ± 0.14 in summer, autumn, spring and winter, respectively. Similarly to AOD, WVC exhibits continuous increasing values from winter to summer peaking at ~5 cm in June–August (Fig. 3b). This annual WVC pattern is characteristic of the Indian monsoon system and may influence the hygroscopic growth of aerosols during the wet summer monsoon, resulting in larger particles and higher AODs (Eck et al., 2010; Kumar et al., 2013; Wu et al., 2015).

In contrast, the monthly variation of α (Fig. 3c) shows larger values in autumn and winter (~1.0 to 1.2); α values decrease till April and then remain nearly unchanged at ~0.2 to 0.4 until August. The lowest α values during April–August indicate a clear dominance of coarse-mode aerosols i.e., dust transported from the deserts of Arabia and southwest Asia (Prasad et al., 2007; Srivastava et al., 2014a) or mixing of dust with marine aerosols produced by the strong sea-surface monsoon winds over the Arabian Sea (Kaskaoutis et al., 2010). The α values of ~1.0 to 1.2 during October–January reveal a rather mixing of fine with coarse-mode aerosols resulting in a bimodal size distribution with equal contribution from fine and coarse particles (Eck et al., 2005), as will be seen in Fig. 6. In general, the monthly variability of α over Desalpar follows the pattern of IGP sites (Singh et al., 2004; Ganguly et al., 2006a, 2006b; Kaskaoutis et al., 2013; Srivastava et al., 2014b) and other locations in south India (Sinha et al., 2013). On seasonal basis, larger α values are found in autumn 1.02 ± 0.27 and winter 0.90 ± 0.27, compared to spring 0.41 ± 0.27 and summer 0.41 ± 0.35. The larger values of $\alpha_{440-675}$ compared to $\alpha_{675-870}$ during March–August, suggest a positive curvature in Eq. ((2) and dominance of coarse particles; the general similarity between values of $\alpha_{440-675}$ and $\alpha_{675-870}$ in November–February indicates a bimodal size distribution with lower curvature and nearly equal contributions from fine and coarse particles (Schuster et al., 2006), as will be seen in Fig. 6.

The hourly seasonal-mean diurnal variability of AOD_{500} and $\alpha_{440-870}$ is shown in Fig. 4a–h. Despite the large scatter shown by the gray areas, the diurnal variations in both parameters reveal a general tendency of increasing values towards the afternoon hours in all seasons, with the most pronounced increases to occur in spring and summer for AOD_{500} and in autumn and winter for $\alpha_{440-870}$. The increase in $\alpha_{440-870}$ during afternoon hours in autumn and winter indicate enhanced contribution of anthropogenic aerosols coming from nearby urban/industrialized centers or agricultural biomass burning that are dispersed and transported over Desalpar in the afternoon hours. Furthermore, the dust plumes in spring and summer usually arrive at the site during noon-to-early afternoon hours following the thermal advection in the hot arid surfaces, thus increasing AOD_{500}, while a neutral (in spring) to slight decreasing (in summer) tendency is shown for $\alpha_{440-870}$ for the same hours. Based on multiyear column-integrated and near-surface aerosol observations over a high-altitude remote site in central Himalayas, (Dumka et al., 2008, 2010, 2015) also found similar diurnal variations in aerosol loading, which is attributed to the evolution of boundary-layer height, dilution and dispersion of pollutants from the polluted IGP to remote site during the afternoon hours.

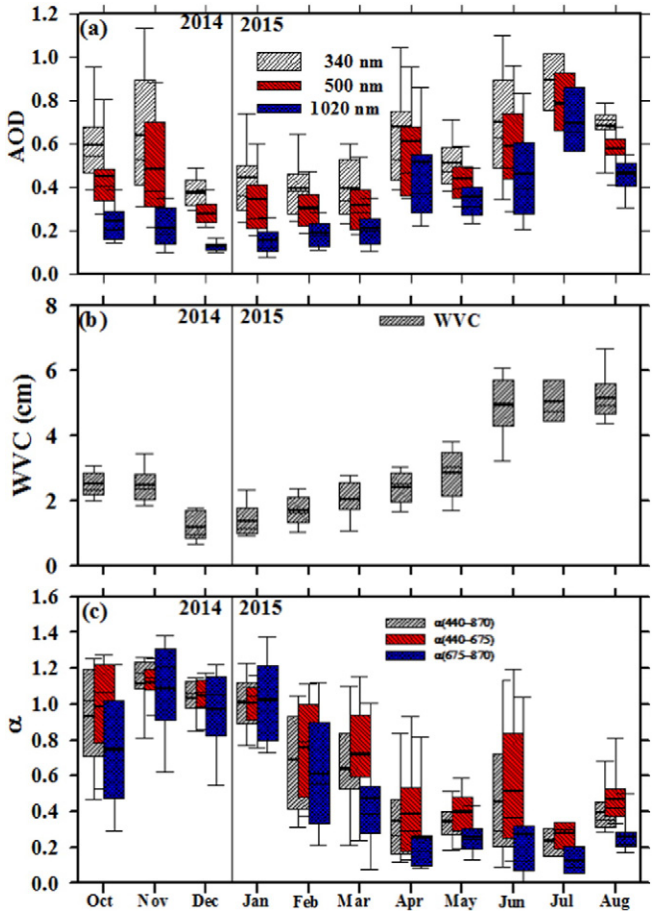

Fig. 3. Monthly variation of spectral AOD at 340 nm, 500 nm and 1020 nm (a), WVC (b) and Ångström-α (c) at three wavelength bands (440–870, 440–675 and 675–870 nm) over Desalpar in Box-Whisker plots. The upper, middle and lower limits in the boxes are the 75th, 50th and 25th percentiles, the bold black line shows the mean value and the vertical bars denote the 95th and 5th percentiles. The vertical line separates 2014 from 2015.

3.2. Frequency distribution of AOD and AE

The frequency distribution of AOD_{500} and $\alpha_{440-870}$ values is shown in Fig. 5a, b, respectively considering all the instantaneous measurements (see Suppl. Table S-1). The frequency distribution of AOD_{500} is shown to be significantly skewed towards lower values peaking at 0.3–0.35 interval, while $AOD_{500} > 1.0$ is rather rare. The AOD_{500} frequency distribution is very well fitted ($R^2 = 0.98$) by a two-mode normal distribution with two peaks centered at 0.306 ± 0.004 and 0.579 ± 0.099 via the formula given by Eq. (9). The bimodal AOD_{500} distribution represents the cases with background or moderate aerosol loading (centered at 0.306) and those under turbid atmospheres (centered at 0.579) (O'Neill et al., 2000):

$$Y = \left(\frac{3.33}{0.21} \times \sqrt{\frac{\pi}{2}}\right) \times \exp\left(-2 \times \left(\frac{x-0.31}{0.21}\right)^2\right) + \left(\frac{1.60}{0.42} \times \sqrt{\frac{\pi}{2}}\right) \times \exp\left(-2 \times \left(\frac{x-0.58}{0.42}\right)^2\right) \quad (9)$$

The frequency distribution of $\alpha_{440-870}$ exhibits a different plot with two distinct modes for the low and high values, indicating a nearly equal contribution from fine and coarse aerosols with a threshold in $\alpha_{440-870}$ of about 0.7 (Fig. 6b). A similar frequency distribution with the presence of two peaks was observed over Hyderabad during spring (Kaskaoutis et al., 2009; Sinha et al., 2012). The $\alpha_{440-870}$ frequency distribution is well represented by a three-mode normal distribution centered at 0.24, 0.56 and 1.09 respectively, according to Eq. (10):

$$Y = \left(\frac{1.55}{0.26} \times \sqrt{\frac{\pi}{2}}\right) \times exp\left(-2 \times \left(\frac{x-0.24}{0.26}\right)^2\right) + \left(\frac{1.61}{0.49} \times \sqrt{\frac{\pi}{2}}\right) \times exp\left(-2 \times \left(\frac{x-0.56}{0.49}\right)^2\right) + \left(\frac{2.24}{0.34} \times \sqrt{\frac{\pi}{2}}\right) \times exp\left(-2 \times \left(\frac{x-1.09}{0.34}\right)^2\right) \quad (10)$$

The first and second $\alpha_{440-870}$ modes (0.24 and 0.56) indicate the dominance of coarse-mode particles over the site, due to its remote location in a semi-arid region close to the Arabian Sea and in proximity to the Thar Desert. The third mode centered at 1.09 indicates the dominance of anthropogenic aerosols and pollution plumes from Indus Valley and urban centers as well as black-carbon aerosols from the thermal/coal power plant in a neighboring area.

3.3. Volume size distribution

The aerosol optical properties obtained from the Sun/sky radiometer are strongly dependent on columnar size distribution, which is closely related to α, α′, fine-mode fraction and its variations (Eck et al., 2010; Sinha et al., 2012). Fig. 6a–e shows the monthly and seasonal mean variations of VSD over Desalpar, while the vertical bars correspond to one standard deviation about the mean. The overall uncertainty in the estimation of the VSDs is ~15% (Kaskaoutis et al., 2013), while the mode radii for the fine (r_1) and coarse (r_2) aerosols are given in each graph. All the months and seasons show bimodal VSDs with distinct fine and coarse modes centered at radius ~0.13–0.18 μm and 2.3–2.8 μm, respectively. In autumn and winter months (Fig. 6a, b), VSD exhibits nearly equal contributions from fine and coarse particles, thus giving AE values in the range 0.9–1.1 (Eck et al., 2005). In these seasons, the contribution of anthropogenic urban/industrial aerosols is significant and affects VSDs (Kar et al., 2010). However, after March the VSDs show a small decrease in the fine mode and an impressive increase in coarse mode (Fig. 6c, d) because of increase in dust and marine aerosols concentration that is reflected by a large decrease in α values at all wavelength bands (Fig. 3c). Although the fine and coarse mode radius of VSDs do not change significantly across the year, the fine-to-coarse mode fraction exhibits pronounced variations, which affects the large variability in $\alpha_{675-870}$ across the year (Fig. 3c). The seasonal variability in VSDs (Fig. 6e) is characteristic of seasonally-varying air masses, aerosol properties, and types and exhibits large similarities to the VSDs found over Kanpur (Singh et al., 2004; Kaskaoutis et al., 2013) and Delhi (Srivastava et al., 2014b). It should also be noted that the fine-mode radii in autumn and winter are slightly higher than those in spring and summer (Fig. 6e), indicating a coagulation of the fine anthropogenic aerosols during October–February.

3.4. SSA

SSA is defined as the ratio of scattering to total extinction (scattering + absorption) of solar radiation due to aerosols and shows the fraction of radiation absorbed by the atmosphere (1-SSA). It is one of the crucial parameters for the estimation of radiative effects of aerosols and may range from 0 (purely absorption) to 1 (purely scattering). The spectral variation of SSA gives useful information about the dominance of specific aerosol types (e.g. black carbon, organic carbon, dust, sulfates) and also can be used in combination with α and/or fine mode fraction (FMF) for the identification of aerosol types (Srivastava et al., 2012, 2014b). In the present study, SSA was retrieved at four wavelengths (440, 675, 870 and 1020 nm) on the daily basis during October 2014–August 2015 and its monthly variation is shown in Fig. 7a. The results reveal a significant fluctuation in both values and spectral

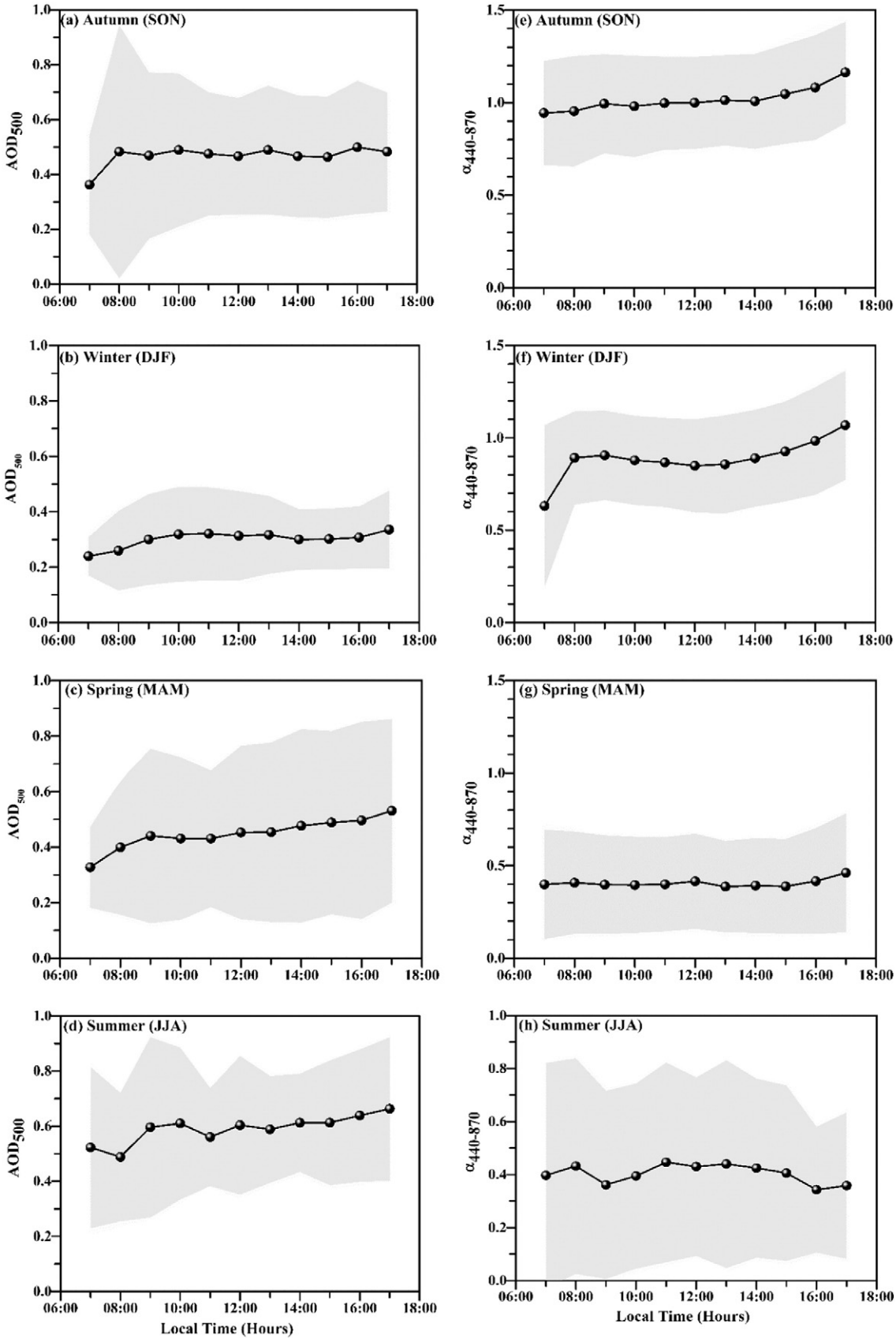

Fig. 4. Seasonal-mean diurnal variations of AOD_{500} (left panels) and $\alpha_{440-870}$ (right panels) over Desalpar in the period October 2014–August 2015. The grey areas denote one standard deviation about the mean.

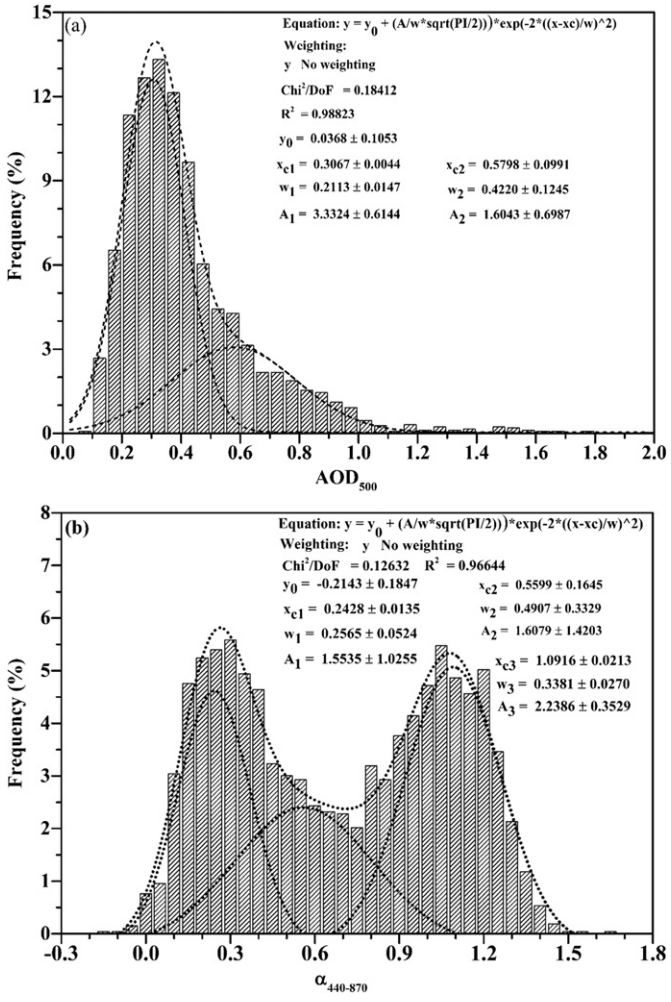

Fig. 5. Frequency distributions of AOD_{500} (a) and Ångström exponent at 440–870 nm (b) at Desalpar during the period October 2014 to August 2015. The dash lines denote the Gauss fitting curves. The fitting equations and the related statistical parameters and correlation coefficients are also given in the graphs.

dependence of SSA around the year, implying significant changes in the dominant aerosol types. From October to January, SSA exhibits small spectral dependence with a slight decrease in longer wavelengths and values ~0.88–0.89, which reverses afterward with a large increase in SSA values, especially at longer wavelengths. SSA increases with wavelength for dust aerosols and decreases for biomass-burning and urban/industrial aerosols, while it exhibits almost neutral spectral dependence in the case of the aerosol mixture and sulfate particles (Dubovik et al., 2002; Russell et al., 2010; Giles et al., 2011, 2012). It was found that SSA at 440 nm (SSA_{440}) varied from 0.84 to 0.95 (mean of 0.89 ± 0.02) with relatively lower values during October–January and increasing from February to August. The much lower SSA_{440} values compared to those at longer wavelengths from March to August are attributed to enhanced absorption by iron oxides under the dominance of dust aerosols (Bergstrom et al., 2007; Derimian et al., 2008; Giles et al., 2012).

The seasonal-mean spectral variation of SSA over Desalpar (Fig. 7b) shows an increasing trend with wavelength in spring and summer due to the influence of dust aerosols, which are highly scattering from the visible to the near-infrared spectrum (Dubovik et al., 2002). In contrast, during autumn and winter, SSA is nearly independent of the wavelength, indicating equal mixing of fine and coarse particles, as was seen in VSDs (Fig. 6). Earlier study by Singh et al. (2004) over Kanpur also found a similar spectral variation in SSA and suggested that the increase in SSA during summer may also be attributed to the hygroscopic growth of water-soluble aerosols under high WVC besides the long-range transport of dust. Using Sun/sky radiometer measurements over Delhi, Pandithurai et al. (2008) reported lower SSA values (0.84 to 0.74 from March to June, respectively) compared to our findings due to mixing of black carbon with dust aerosols over the urban environment. Moorthy et al. (2007) have also reported that the SSA for dust aerosols was in the range of 0.88–0.94, while the dust over the Thar Desert was more absorbing in nature compared to pure dust due to black carbon (BC) contamination. Based on ground-based Sun photometer observations during spring, Dumka et al. (2014) also reported lower SSA values of 0.86–0.88 over Pantnagar, Bareilly and Kanpur sites in IGP. Furthermore, the mean SSA spectral dependence is examined for two groups during the study period (Fig. 7c) differentiated by the threshold of $\alpha_{440-870} = 0.8$ for the coarse and fine-mode aerosols (Eck et al., 2005, 2010). The results reveal a significant difference in the spectral variation of SSA between the two modes. The coarse mode exhibits an increase in SSA spectrum with wavelength, while for $\alpha > 0.8$ a rather negligible spectral dependence of SSA is shown corresponding to well-mixed aerosols with a significant anthropogenic contribution.

In order to assess the absorbing aerosols and to associate their absorbing capability with the aerosol size, we analyzed the differences between SSA at 440 nm and 1020 nm ($d_{SSA} = SSA_{440\ nm} - SSA_{1020\ nm}$) and correlated them with α for three levels of SSA_{1020} (Fig. 7d) following Derimian et al. (2008). It should be noted here that α and SSA are daily-mean values on days with the availability of SSA retrievals. Furthermore, this plot has main advantages as the spectral distribution of SSA is characterized by a single parameter (d_{SSA}), and secondly, d_{SSA} provides a better accuracy than the absolute SSA values since the retrieval of spectral SSA dependence is more reliable than that of absolute values (Derimian et al., 2008; Dumka et al., 2014). It is seen that as α gradually increases from 0.1 to 1.4 (i.e. the contribution of fine aerosols increases), the spectral SSA changes from stronger absorption at 440 nm (negative d_{SSA}) to stronger absorption at 1020 nm (positive d_{SSA}). For coarse-mode aerosols ($\alpha_{440-870} < \sim 0.4$), the absorption at 1020 nm is quite low since SSA > 0.95 values dominate (blue circles in Fig. 7d). In contrast, for $\alpha_{440-870}$ values above 1.0, there is increased absorption at both 440 nm (positive d_{SSA}) and 1020 nm ($SSA_{1020} < 0.9$, black points in Fig. 7d); this could be attributed to the mixture of dust with anthropogenic aerosols and pollutions. d_{SSA} values of ~−0.1 suggest the dominance of iron oxides in desert dust aerosols (Dumka et al., 2014) and can be approached only for the lowest $\alpha_{440-870}$ values (Fig. 7d).

The spectral absorption optical depth (AAOD; $\tau_{abs\lambda}$) has been computed from the extinction AOD ($\tau_{ext\lambda}$) and SSA (ω_0) following previous studies (i.e., Bergstrom et al., 2007; Russell et al., 2010; Dumka et al., 2014), as below:

$$\tau_{abs}(\lambda) = [1-\omega_0(\lambda)] \times \tau_{ext}(\lambda) \quad (11)$$

Eq. (11) provides useful information about the optical properties of absorbing aerosols. Using the Ångström power law ($AAOD(\lambda) = K\lambda^{-AAE}$), where K is the aerosol loading, the absorption Ångström exponent (AAE) has been computed by the negative slope of a log-log plot of AOD versus wavelength as $AAE = -d\ln[\tau_{abs}(\lambda)]/d\ln(\lambda)$. The monthly-mean variation of the spectral AAOD along with AAE in three different bands (440–870 nm, 675–870 nm, and 440–675 nm) are given in Supplementary material (See Suppl. Fig. S-3 a, b), respectively. Both AAOD and AAE revealed significant monthly variation, ranging between 0.02 and 0.25 (average of 0.05 ± 0.03 for $AAOD_{440}$) and 0.27 – 2.27 (average of 1.13 ± 0.38 for $AAE_{440-870}$). AAOD was found to exhibit slightly larger values (~0.05–0.07) in October, April and June (especially at 440 nm), indicating enhanced absorption either by biomass-burning aerosols in October or dust during spring. On the other hand, the larger values of AAOD correspond to dust and organic aerosols or mixes between them (~>1.5), which absorb strongly in the ultraviolet but not in visible and near-infrared; AAE values ~1.0 reveal presence of BC aerosols, which show a strong absorption throughout the solar spectrum (Bergstrom et al., 2007; Russell et al., 2010). Therefore, the larger AAE

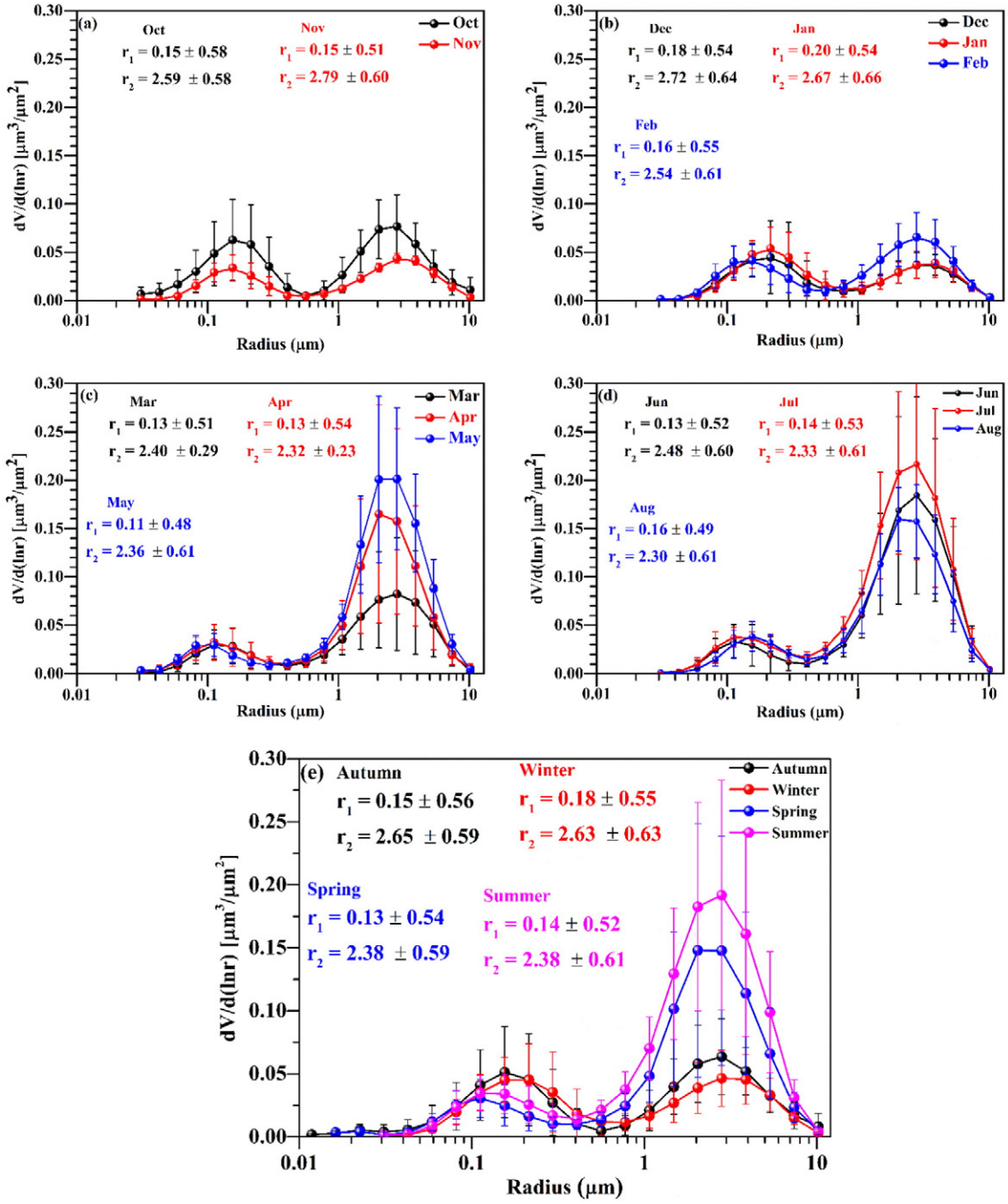

Fig. 6. Monthly and seasonal-mean volume aerosol size distribution over Desalpar during the period October 2014– August 2015. The mode-radius for the fine (r_1) and coarse (r_2) modes are given in each graph.

values in the spring and summer months (Suppl. Fig. S-3b) indicate the absorption by dust, also mixed with other aerosols, in the shorter wavelengths, while the peak in November implies the presence of long-range transported biomass-burning aerosols from Punjab agricultural fires in the northern part of the Indus Valley (Kaskaoutis et al., 2014). The AAE monthly means of ~1.0 in December–February suggest that the absorbing aerosols over Desalpar are mainly composed of BC emitted from the nearby thermal (coal) power plant and urban areas.

3.5. Aerosol classification and types

A preliminary identification of the main aerosol types over Desalpar is attempted via the common technique of AOD_{500} vs $\alpha_{440-870}$ relationship (Pace et al., 2006; Kaskaoutis et al., 2009, 2011b; Kumar et al., 2014, 2015b; Bibi et al., 2016; Yu et al., 2016). This relationship was preferred against others, like SSA vs FMF (Srivastava et al., 2012, 2014b) or AAE vs scattering α (Bergstrom et al., 2007; Russell et al., 2010; Giles et al., 2012) due to larger availability of AOD_{500} and α values from instantaneous measurements and not daily-averages as per the case of SSA, AAE, FMF (see Suppl. Table S-1). The scatter plot between AOD_{500} and $\alpha_{440-870}$ using all instantaneous measurements is shown in Fig. 8a. The data scatter is characteristic for the presence of various aerosol types over Desalpar (e.g. biomass burning, urban-industrial, desert dust and clean-maritime), as found over several sites in India, like Hyderabad (Kaskaoutis et al., 2009), Dibrugarh (Pathak et al., 2012), Pune (Vijayakumar and Devara, 2013), Delhi and Kanpur (Kaskaoutis et al., 2012) as well as over Arabian Sea (Kaskaoutis et al., 2010) and Bay of Bengal (Kaskaoutis et al., 2011b). More specifically, $\alpha_{440-870}$

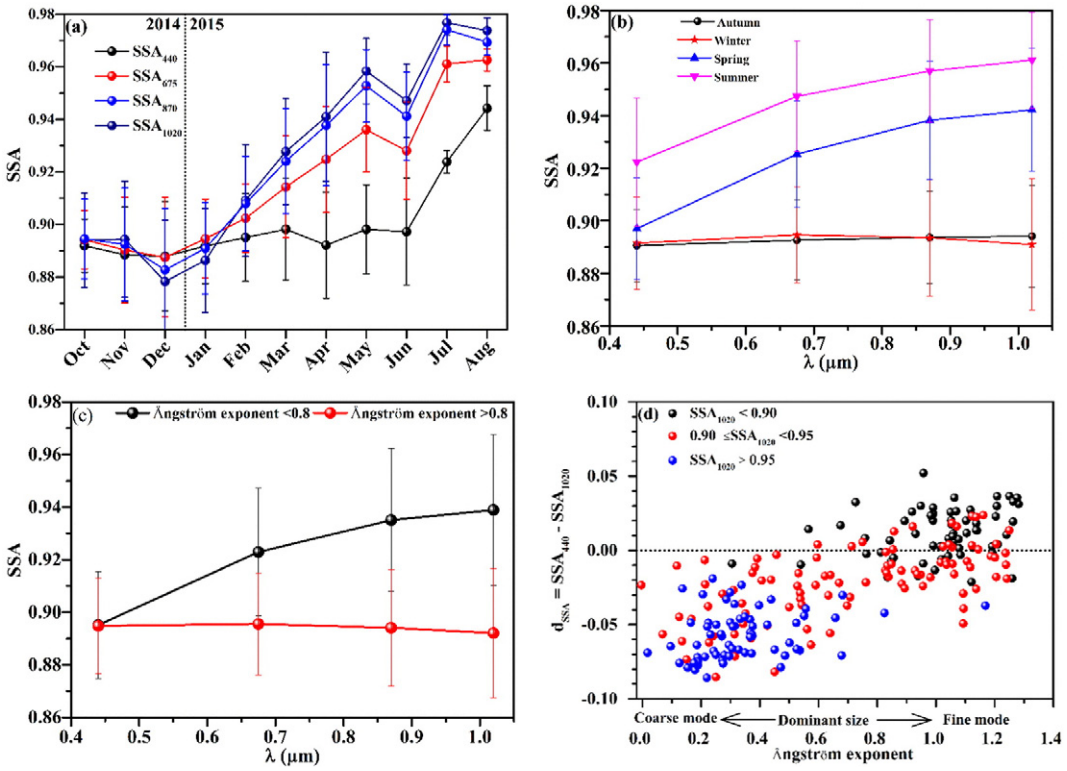

Fig. 7. (a) Monthly-mean variation of SSA at four wavelengths (440, 675, 870 and 1020 nm), (b) seasonal-mean spectral variation of SSA, (c) mean spectral variation of SSA for cases with $\alpha_{440-870}$ above and below 0.8 and, (d) difference of SSA [$d_{SSA} = SSA_{440}-SSA_{1020}$] versus $\alpha_{440-870}$ for different ranges of SSA_{1020} over Desalpar in the period October 2014 to August 2015. The vertical bars correspond to one standard deviation about the monthly mean.

presents a large range (~0.1 to 1.4) for $AOD_{500} < 0.3$, characteristic of several aerosol types mixed into the atmosphere. For $AOD_{500} > 0.5$–0.6, $\alpha_{440-870}$ usually takes either large (>1.0) or small (<0.6) values corresponding to turbid conditions caused by biomass-burning or desert-dust aerosols, respectively. For quantifying the contribution of the major aerosol types, some threshold values were taken. More specifically, clean continental (CC) aerosols representing the background conditions over Desalpar are considered as having $AOD_{500} < 0.3$ and $\alpha_{440-870} > 1.0$, while marine-influenced aerosols (Mar) are for $AOD_{500} < 0.3$ and $\alpha_{440-870} < 0.9$. Cases corresponding to turbid atmospheres dominated by transported biomass-burning aerosols or thick urban/industrial plumes (BB/UI) are for $AOD_{500} > 0.6$ and $\alpha_{440-870} > 1.0$, while desert-dust aerosols (DD) are characterized by $AOD_{500} > 0.6$ and $\alpha_{440-870} < 0.6$ (Fig. 8a). Cases that do not belong to any of the above categories are characterized as mixed aerosols (Mix), which are found to be the majority (56.3%) (Fig. 8b). Furthermore, marine-influenced aerosols hold a significant fraction over the site (18.2%) due to its neighboring to the Arabian Sea, while the influence of BB/UI aerosols is limited (5.7% of the cases). Indeed, the smoke plumes from the agricultural crop-residue burning in the north part of the Indus Valley were found to marginally affect the study region (Kaskaoutis et al., 2014). Due to the neighboring to the Thar Desert and arid regions in southwest Asia that emit large amounts of dust covering the whole area during spring and summer, the DD aerosols possess an important fraction of 10.6%, while CC conditions over Desalpar are observed at 9.1% of the cases. Comparison of the present results with those from other studies over India is not an easy task due to the different threshold values selected for specific aerosol types that may significantly differentiate the results.

Furthermore, the modification of aerosol properties over Desalpar is examined using the graphical scheme proposed by Gobbi et al. (2007), which combines α and its spectral variation (dα) with the fine-mode radii (R_f) and fine-mode fraction (η) as grid parameters in grouped AOD. Therefore, the change in α, dα ($\alpha_{40-675}-\alpha_{675-870}$) pairs with increasing AOD_{500} provides valuable information about several aerosol modification processes in the atmosphere (i.e. coagulation, humidification, addition of fine/coarse particles), as examined in a series of previous studies (e.g., Gobbi et al., 2007; Kaskaoutis et al., 2010, 2011b, 2014; Sinha et al., 2012; Kumar et al., 2014). In the present case (Fig. 9a, b), the aerosol modification processes are examined separately for October–February and March–August due to differing aerosol properties dominated by fine/mixed and coarse-mode aerosols, respectively.

In Fig. 9a, increasing AOD is associated with the increase in η, which is usually above 70% for $AOD_{500} > 0.9$ (except few cases). This indicates that the turbid atmospheres during the autumn-winter period are characterized by addition of fine-mode particles i.e., anthropogenic pollution and/or biomass smoke. A concurrent slight increase in R_f (from ~0.15 μm to ~0.18 μm) is also shown for these high-AOD data points, suggesting coagulation of the fine particles under turbid atmospheres. Similar modifications in the fine-mode fraction and R_f for increasing AOD were also found for aerosols over urban Hyderabad (Sinha et al., 2012) and polluted sites in IGP under the influence of biomass smoke (Kaskaoutis et al., 2014), as well as over the northern region of the Bay of Bengal (Kaskaoutis et al., 2011b) in autumn and winter, indicating that such modifications tend to be a general feature over India during the cold period. The few cases with high AODs and low η < 30% correspond to the impact of rare dust plumes over the site in October (see Fig. 2). In contrast, during the period March–August, the vast majority of the data points exhibit η values <50% or even <30% and $\alpha_{440-870}$ usually below 0.8 suggesting the clear dominance of coarse-mode aerosols (Fig. 9b). Increasing of AOD leads to a shift of the data points toward the origin (α, dα = 0) along a R_f curve of ~0.10–0.12 μm and continuously decreasing values of η, indicating negligible variation in fine-mode radii and a significant increase in the coarse-mode fraction. Especially for cases with $AOD_{500} > 1.2$, the η is below 20% and the R_f may increase to 0.2–0.3 μm suggesting nearly absence of fine mode. These conditions are characteristic for environments strongly impacted by intense dust storms and present great similarity to those found over Kanpur during such episodes (Kaskaoutis et al., 2012).

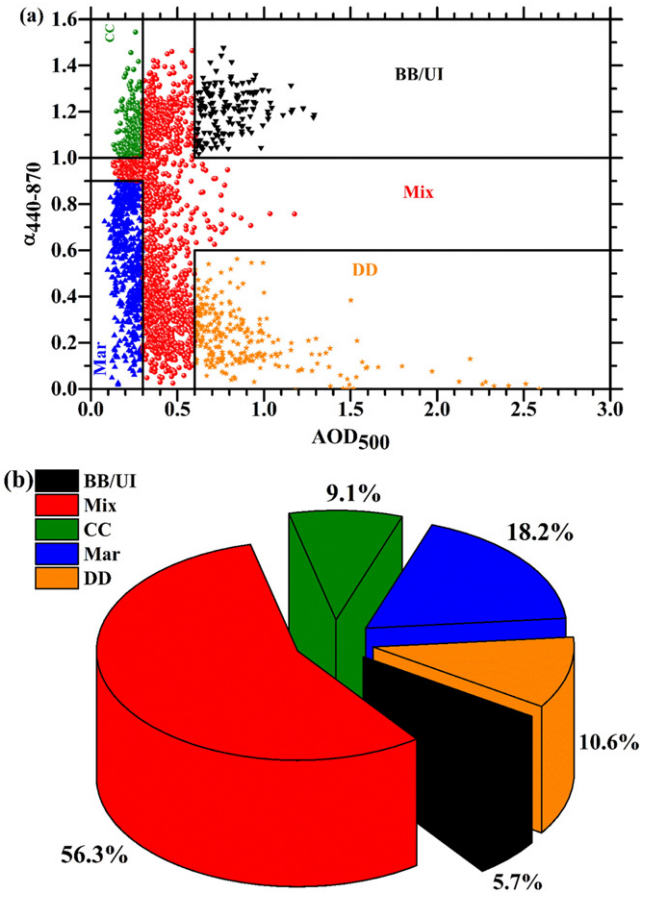

Fig. 8. Scatter plot of AOD_{500} versus $\alpha_{440-870}$ nm for identification of the dominant aerosol types (a) and percentage of each aerosol type (b) over Desalpar in the period October 2014 to August 2015. The labels stand as CC: Continental Clean; Mar: Marine; BB/UI: Biomass Burning/Urban Industrial; DD: Desert Dust and Mix: Mixed type aerosols.

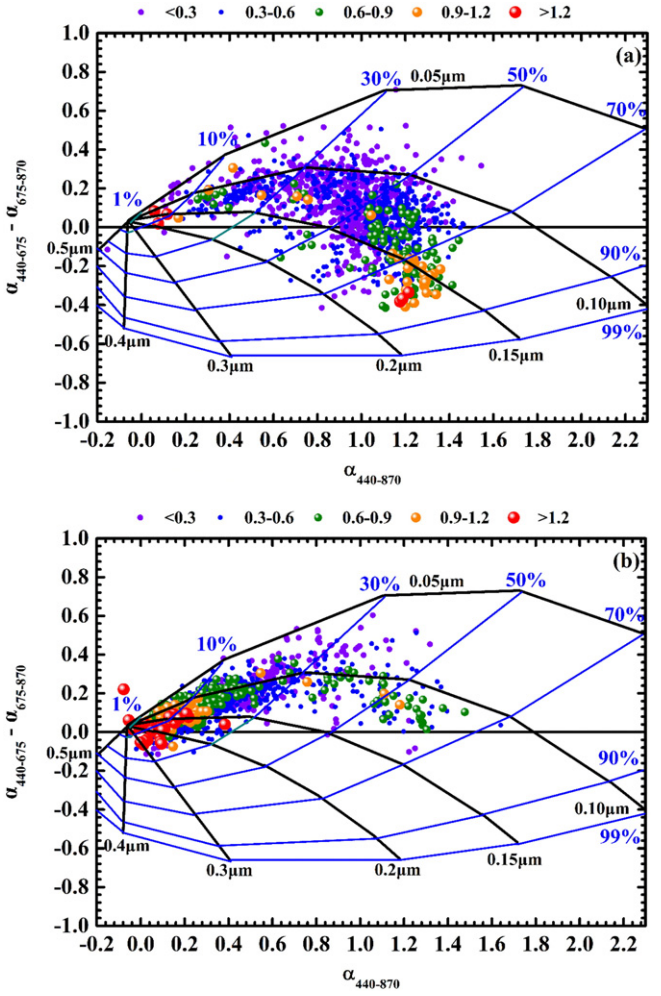

Fig. 9. Ångström exponent difference, $d\alpha = \alpha_{440-675} - \alpha_{675-870}$, as a function of $\alpha_{440-870}$ and AOD_{500} (color scale) over Desalpar for the periods October–February (a) and March–August (b). The black lines indicate the fixed fine-mode radius (R_f) and the blue lines the fixed fine-mode fraction (η). The size of the circle denotes the AOD_{500} values.

3.6. Curvature effects on AOD and AE

As discussed in Section 2.2, the aerosol size distribution is bimodal or multi-modal in nature; therefore, the AOD vs wavelength in log-log co-ordinates departs from linearity and is best-simulated by a 2nd-order polynomial fit (Eq. ((2)). The inclusion of curvature, which is quantified by a_2, helps in better identification of the aerosol types in conjunction with AOD and α (Eck et al., 1999, 2005; Schuster et al., 2006; Kaskaoutis et al., 2007, 2011b). In Fig. 10a–f, AOD_{500} and $\alpha_{440-870}$ are correlated with a_2 (Eq. ((2)), a_2–a_1 (Eq. ((2)) and α' (Eq. (5)) revealing valuable information for the identified aerosol types.–

a_2 indicates whether fine or coarse-mode aerosols are dominant in the size spectrum, with positive values suggesting higher concentrations of coarse-mode aerosols and negative values indicating higher loading of fine-mode aerosols (Eck et al., 1999, 2005; Kaskaoutis et al., 2007). Values of a_2 close to zero are mostly shown for bimodal size distributions with similar fine- and coarse-mode contributions (Eck et al., 1999, 2005). In our case, a_2 exhibits large scatter from −0.6 to 0.7, revealing that the curvature is significant in the vast majority of the cases (Fig. 10a, b). As expected, the a_2 values are mostly negative for the fine BB/UI and CC aerosols and positive for the large marine and dust particles, giving credit to the aerosol type discrimination method (Fig. 9a). Note also that as AOD_{500} increases, the a_2 values for DD tend to zero, as was also found for dust aerosols in Solar Village, Saudi Arabia; furthermore, the BB/UI aerosols show large negative a_2 values, as was found over Alta Floresta, Brazil which is severely affected by seasonal biomass burning (Kaskaoutis et al., 2007). The scatter plot between a_2 and $\alpha_{440-870}$ (Fig. 10b) shows great similarities to those found in Fig. 9, since a_2 is proportional to $d\alpha$ (Schuster et al., 2006; Kaskaoutis et al., 2007). Thus, combining Fig. 9 and Fig. 10b, one can note that the BB/UI aerosols correspond to negative $d\alpha$ and high η, while the DD particles in Fig. 10b are shifted towards the origin of the Gobbi's scheme (Fig. 9) with α, $d\alpha$ close to zero.

Schuster et al. (2006) suggested that $a_2 - a_1$ equals to α, while Kaskaoutis et al. (2007) noted that this approximation is valid when these parameters correspond to the same wavelength range. As can be seen from Fig. 10d, the a_2–a_1 vs $\alpha_{440-870}$ data points lie upon the $y = x$ line ($R^2 = 0.998$), suggesting very high accuracy in the retrievals of the spectral AOD and α. Therefore, the a_2–a_1 vs AOD_{500} scatter plot (Fig. 10c) is similar to Fig. 8a. Finally, as $\alpha' = -2a_2$, the findings that are extracted from Fig. 10e and f are same with those from Fig. 10a and b, respectively. Therefore, the DD aerosols correspond to negative α' and BB/UI to positive α' as also found in previous studies (Eck et al., 1999, 2005; Kaskaoutis et al., 2007; Kumar et al., 2013; Kedia et al., 2014).

3.7. Aerosol transport

Fig. 11 illustrates the mean transport pathways and source regions of aerosols based on 5-day air-mass back trajectories at 12 UTC (+5:30 LST) ending over Desalpar at three altitudes (500 m, 1000 m, and

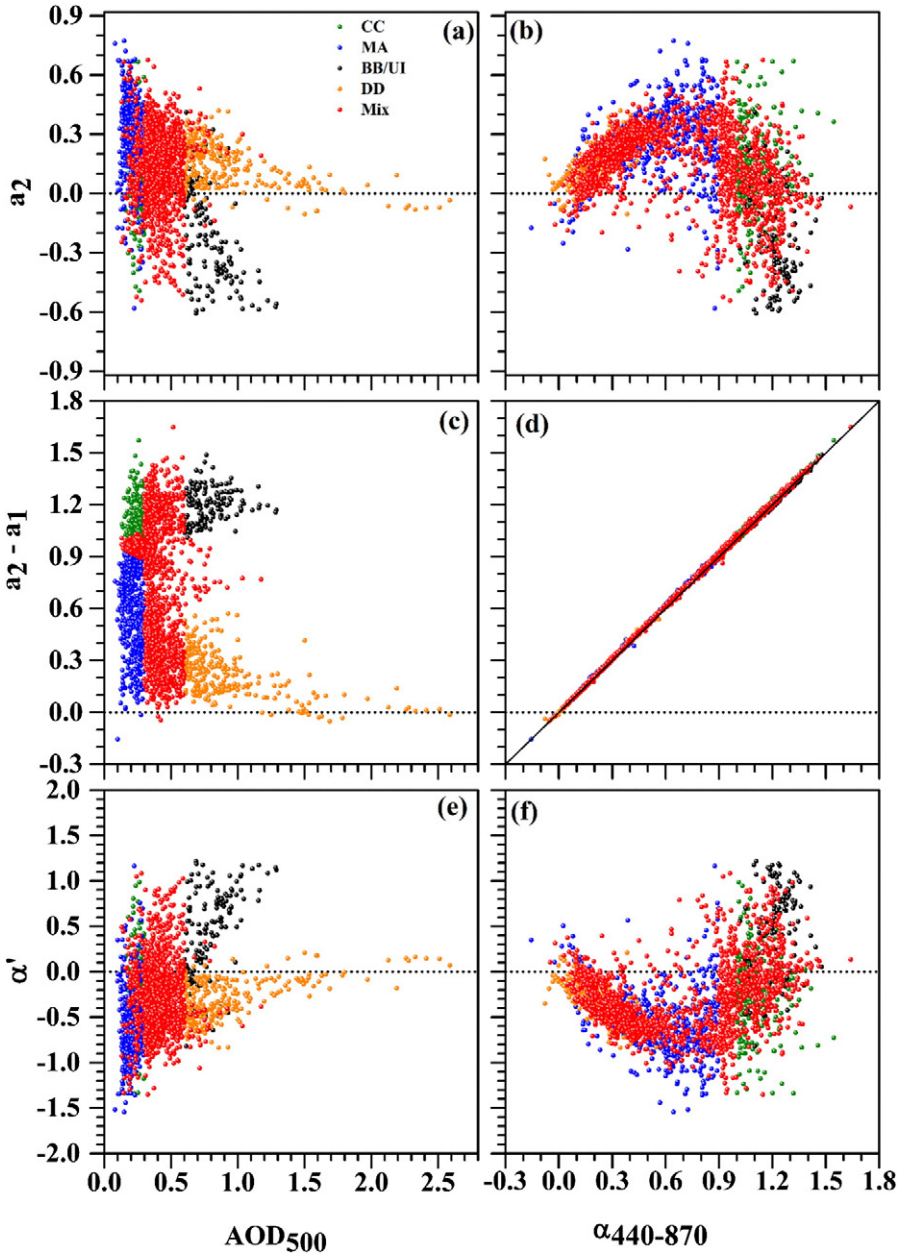

Fig. 10. Scatter plots between the curvature a_2, difference of polynomial coefficients a_1 and a_2 ($a_2 - a_1$), and derivative of Ångström exponent (α') versus AOD_{500} (left panels) and $\alpha_{440-870}$ (right panels) over Desalpar in the period October 2014 to August 2015.

4000 m above ground level) by using the HYSPLIT model, as described in Section 2.5. At 500 m, the trajectories are mostly of local origin (43%) enriched with aerosols from the Thar Desert, urban areas and Indus Valley, while a large fraction (30%) corresponds to air-masses coming from Arabia and southwest Asia carrying dust aerosols in certain circumstances. 22% of the cases at 500 m and 4% at 1000 m are associated with the southwest monsoon, favoring the presence of marine aerosols from southwest Arabian Sea mixed with dust during spring and summer. On the other hand, the local air-masses coming from Indus Valley are dominant (59%) at 1000 m, while an important fraction of 23% originates from the Arabian Peninsula (Fig. 11). Air masses from very long distances i.e., Sahara, Mediterranean Basin, Middle East are mostly seen at 4000 m, while their frequency is very limited at lower levels. Table 1 summarizes the aerosol properties for each trajectory cluster and altitude, revealing that the air masses coming from the Arabian Sea at 500 m (cluster 3) show the highest AOD_{500} (0.54 ± 0.33) and lowest $\alpha_{440-870}$ (0.39 ± 0.25) values indicating large influence from the dust accumulated over the Arabian Sea during the summer season (Kaskaoutis et al., 2011a). The air-masses belonging to the local sector (cluster 1) exhibit the largest $\alpha_{440-870}$ values of 0.95 ± 0.26 and 0.86 ± 0.36 for both 500 m and 1000 m, respectively, while those originating from Arabia, Middle East and the Arabian Sea exhibit $\alpha_{440-870}$ usually below 0.5. As expected, the Arabian Sea air masses (cluster 3) are the most humid with the largest WVC for both 500 and 1000 m, while the continental ones (cluster 1) the most dry. The SSA_{675} values do not exhibit large variations between the trajectory clusters; however, the local sector (cluster 1) exhibits slightly lower SSA indicating larger absorption from aerosols from the urban and continental origin.

3.8. DARF

The diurnally-averaged DARF at SFC, TOA and ATM was estimated using the measured aerosol optical properties and SBDART model as

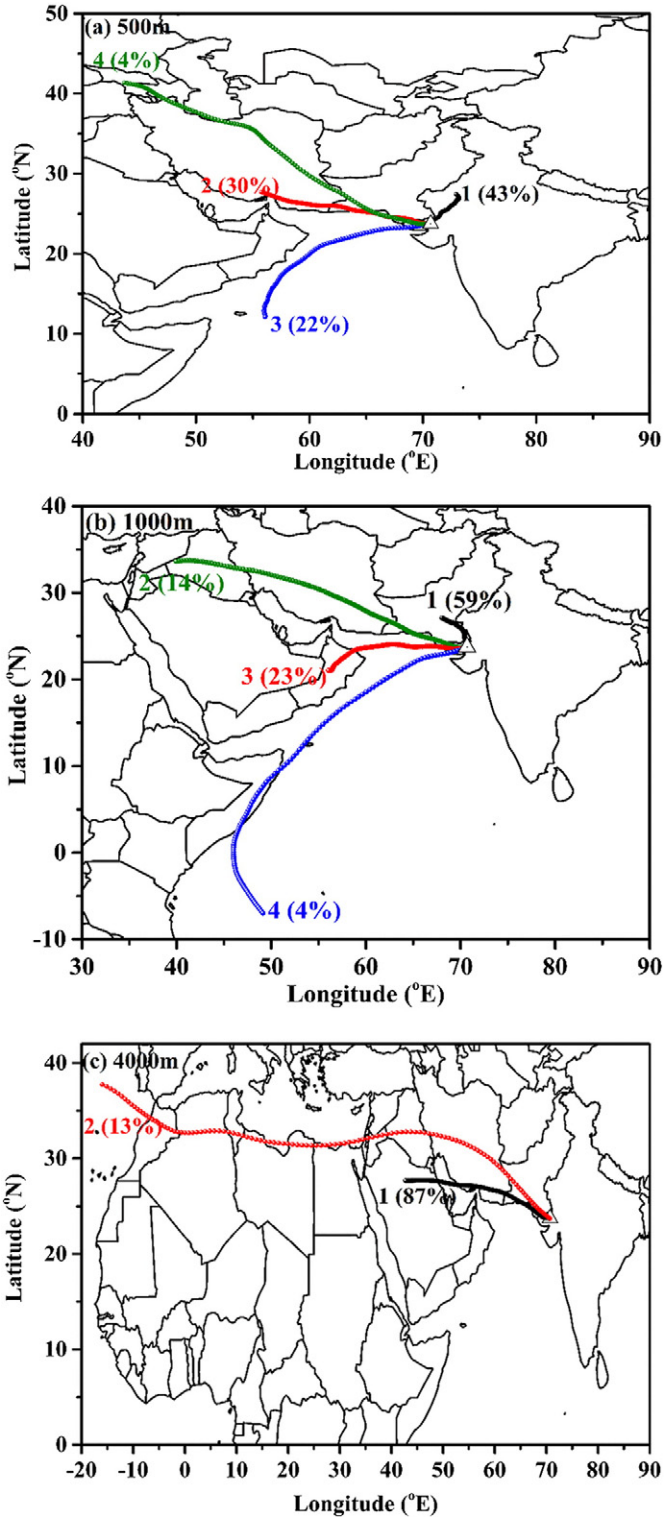

Fig. 11. HYSPLIT-model computed mean trajectory pathways for 5-days air masses ending over Desalpar at 500 (a), 1000 (b) and 4000 (c) meters in the period October 2014 to August 2015. The trajectories correspond to different clusters at each altitude.

described in Section 2.4. The monthly-mean DARF values along with the atmospheric HR were computed from the daily ones and their variation is shown in Fig. 12. DARF at SFC, TOA, and ATM shows significant variability across the year varying from -27.08 W m^{-2} (July) to -10.74 W m^{-2} (December) (mean of -18.42 ± 6.57 W m^{-2}) at TOA, while at SFC DARF ranges from -52.21 W m^{-2} (June) to -21.71 W m^{-2} (December) with a mean value of -35.01 ± 10.97 W m^{-2}. The resultant ATM forcing ranges from 10.97 W m^{-2} (December) to 26.54 W m^{-2} (April) with a mean value of 16.59 ± 5.40 W m^{-2}. DARF at SFC is mostly a function of AOD_{500}, while DARF at TOA depends strongly on SSA, except AOD_{500}, and on the underlying surface albedo (Chand et al., 2009). Both TOA and SFC DARF values are more negative during spring and summer indicating the significant decrease of solar radiation reaching the ground and net radiative cooling due to dust aerosol over the observational site. These DARF values are somewhat lower compared to those found over urban sites in IGP, also affected by dust during the spring-summer period, like Delhi (Ganguly et al., 2006b), Kanpur (Kaskaoutis et al., 2013; Srivastava and Ramachandran, 2013), Gandhi College (Srivastava and Ramachandran, 2013), Ahmedabad (Ramachandran and Kedia, 2010), Patiala (Sharma et al., 2012), where DARF values at surface were found to range between about -50 W m^{-2} to about -80 W m^{-2}. Over these sites the atmospheric radiative forcing and HR values were also larger compared to those found over Desalpar due to much higher contribution of anthropogenic aerosols (Dey and Tripathi, 2008). Furthermore, the ratio (F) $DARF_{SFC}/DARF_{TOA}$ was found to range from 1.52 to 2.23 with a mean value of 1.94 ± 0.20 during the study period suggesting dominance of scattering aerosols over Desalpar (Satheesh and Ramanathan, 2000; Sinha et al., 2013; and references therein). The atmospheric heating rates due to $DARF_{ATM}$ are found to vary between 0.31 K day^{-1} (December) and 0.75 K day^{-1} (April) with a mean value of 0.47 ± 0.15 K day^{-1} during the study period, lower than the values (0.7–1.2 K day^{-1}) reported over the Thar Desert (Moorthy et al., 2007). Table 1 summarizes the DARF and HR values for each trajectory cluster and altitude without revealing significant differences between them. However, larger DARF values at SFC, TOA and ATM are found for cluster 3 at 500 m (due to much larger AOD_{500}), while more negative (less positive) DARF values at TOA (ATM) are seen for cluster 4 at 1000 m, indicating more scattering aerosols compared to the rest of the clusters (note the larger AOD_{500} and SSA_{675} for this trajectory cluster in Table 1).

4. Conclusions

The present study analyzed for the first time the aerosol optical and physical properties and radiative forcing over Desalpar, western India, and a remote site located in the vicinity of northeastern Arabian Sea, Thar Desert and Indus Valley. The analysis was based on ground-based Sun/sky radiometric measurements, which were used to obtain spectral AOD, Ångström exponent, and their wavelength dependence as well as intensive aerosol properties like volume size distribution and SSA during the period October 2014 to August 2015. The aerosol characteristics were examined on daily, monthly and seasonal basis and the major findings are summarized below:

1. The daily-averaged values of AOD_{500} and $\alpha_{440-870}$ varied from 0.13 to 2.39 and from ~0.02 to 1.35 with annual means of 0.43 ± 0.26 and 0.69 ± 0.39, respectively. On the seasonal basis, AOD_{500} exhibited higher values in summer (0.61 ± 0.34) followed by autumn (0.47 ± 0.26), spring (0.45 ± 0.30) and winter (0.31 ± 0.14), while the low α values in spring and summer indicate the dominance of coarse-mode dust aerosols, also mixed with marine particles. In contrast, the higher (around 1–1.2) α values in autumn and winter, indicated the presence of mixed aerosols with significant anthropogenic contribution from the Indus valley and urban/industrialized centers. On diurnal basis, both AOD_{500} and α were found to exhibit a slight increase from morning to afternoon due to spreading of aerosols from other areas over the monitoring site.
2. The analysis of VSDs and spectral SSA on monthly and seasonal basis justified the enhanced presence of dust during the period March–August, while from October to February the aerosol field could be mostly characterized as mixed with nearly equal contributions of fine and coarse-mode particles in VSDs.

Table 1
Summary of the values of AOD_{500}, $\alpha_{440-870}$, WVC, SSA_{675}, DARF at TOA, SFC and ATM and heating rate for the different trajectory clusters at 500 m, 1000 m, and 4000 m levels. Values in parenthesis correspond to one standard deviation about the means.

Cluster	Traj. No. # (%)	Aerosol optical properties			WVC (±SD)	Direct aerosol radiative forcing ($W m^{-2}$)			Heating rate ($K day^{-1}$)
		$AOD_{500\ nm}$ (±SD)	$\alpha_{440-870}$ (±SD)	$SSA_{675\ nm}$ (±SD)		TOA	SFC	ATM	
Trajectories at 500 m above ground level									
1	97 (43%)	0.36 (±0.18)	0.95 (±0.26)	0.89 (±0.02)	1.70 (±0.75)	−14.12	−29.17	15.06	0.42
2	67 (30%)	0.37 (±0.19)	0.58 (±0.34)	0.89 (±0.02)	2.15 (±0.72)	−16.04	−31.04	15.00	0.42
3	50 (22%)	0.54 (±0.33)	0.39 (±0.25)	0.90 (±0.02)	3.08 (±1.11)	−22.49	−40.17	17.69	0.50
4	10 (4%)	0.36 (±0.23)	0.42 (±0.27)	0.89 (±0.02)	1.84 (±1.09)	−14.60	−30.44	15.84	0.45
Trajectories at 1000 m above ground level									
1	133 (59%)	0.37 (±0.19)	0.86 (±0.32)	0.89 (±0.02)	1.83 (±0.77)	−14.86	−30.48	15.62	0.44
2	32 (14%)	0.47 (±0.42)	0.37 (±0.25)	0.89 (±0.02)	2.11 (±0.92)	−19.77	−38.56	18.79	0.53
3	51 (23%)	0.42 (±0.17)	0.50 (±0.32)	0.90 (±0.02)	2.57 (±0.83)	−17.83	−32.80	14.97	0.42
4	08 (4%)	0.61 (±0.06)	0.36 (±0.15)	0.94 (±0.01)	4.86 (±0.77)	−25.70	−37.69	11.99	0.34
Trajectories at 4000 m above ground level									
1	194 (87%)	0.40 (±0.18)	0.68 (±0.37)	0.89 (±0.02)	2.23 (±1.03)	−16.53	32.48	15.95	0.45
2	30 (13%)	0.42 (±0.45)	0.74 (±0.38)	0.90 (±0.02)	1.64 (±0.63)	−18.14	−36.11	17.97	0.51
All	224	0.43 (±0.26)	0.69 (±0.39)	0.89 (±0.02)	2.15 (±1.00)	−16.73	−32.98	16.25	0.46

3. SSA was found to significantly increase with the wavelength during March–August (dust aerosols), whereas it obtained lower values (around 0.89) and almost wavelength-independence (mixing of continental aerosols with anthropogenic pollution) during October–February.
4. Via the relationship AOD_{500} vs $\alpha_{440-870}$, a first identification of the main aerosol types was attempted. The results revealed a dominance of the mixed-type aerosols (~56%), with an important contribution of marine-influenced particles (~18%) and desert dust (~10%). Long-range transported aerosols from biomass burning or intensely polluted plumes corresponded to 5.7% of the cases, with the rest (~9%) to correspond to continental background conditions over Desalpar.
5. The inclusion of the spectral dependence of α and the use of a visualization scheme for examining the modification processes in the atmosphere showed that the increase in AOD_{500} during October–February is associated with fine-mode aerosol emissions and increase in fine-mode fraction. In contrast, the increase in AOD_{500} during March–August is related to strong decrease in α and increase in coarse fraction suggesting dominance of dust aerosols.
6. Five-days back trajectories identified four main sectors for the aerosol transport over the monitoring site, with the local sector to contribute more to the presence of fine and more-absorbing aerosols. Long-range transported air masses from the Middle East and southwest Asia contributed more to the presence of dust over Desalpar, while the air masses traversing the Arabian Sea before reaching Desalpar were rich in marine aerosols and dust.
7. DARF estimates over Desalpar were found to range from −27.08 W m^{-2} to −10.74 W m^{-2} and from −52.21 W m^{-2} to −21.71 W m^{-2} at TOA and surface, respectively with the atmospheric forcing varying between 10.97 W m^{-2} and 26.54 W m^{-2} resulting in atmospheric heating rates of 0.31–0.75 K day^{-1}.

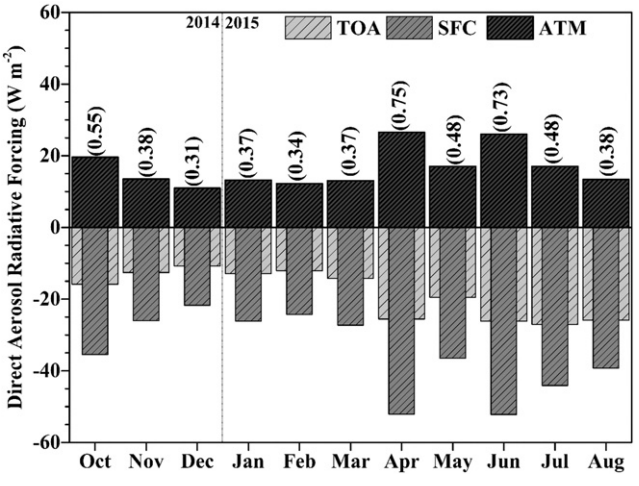

Fig. 12. Monthly variation of DARF values at TOA, SFC and ATM over Desalpar in the period October 2014 to August 2015. The vertical line separates 2014 from 2015.

Acknowledgements

The authors gratefully acknowledge the constant encouragement received from the Director, SAC for carrying out the present research work. Valuable suggestions received from Deputy Director, EPSA, and Head, Calibration & Validation Division also gratefully acknowledged. We are thankful to the team members at Desalpar Cal-Val site for data collection support. Authors also acknowledge the use of HYSPLIT model of NOAA-ARL for air mass back-trajectory analysis and MODIS for surface albedo data used in this work. The authors are thankful to the Editor Prof. Jianmin Chen and two anonymous reviewers whose insightful comments and suggestions helped to considerably improve the scientific quality of the manuscript.

Appendix A. Supplementary data

Supplementary data to this article can be found online at http://dx.doi.org/10.1016/j.scitotenv.2016.09.023.

References

Alam, K., Trautmann, T., Blaschke, T., 2011. Aerosol optical properties and radiative forcing over mega city Karachi. Atmos. Res. 101, 773–782.
Alam, K., Trautmann, T., Blaschke, T., 2012. Aerosol optical and radiative properties during summer and winter seasons over Lahore and Karachi. Atmos. Environ. 50, 234–245.
Alam, K., Trautmann, T., Blaschke, T., Subhan, F., 2014. Changes in aerosol optical properties due to dust storms in the Middle East and Southwest Asia. Remote Sens. Environ. 143, 216–227.
Babu, S.S., Manoj, M.R., Moorthy, K.K., Gogoi, M.M., Nair, V.S., Kompalli, S.K., Satheesh, S.K., Niranjan, K., Ramagopal, K., Bhuyan, P.K., Singh, D., 2013. Trends in aerosol optical depth over Indian region: potential causes and impact indicators. J. Geophys. Res. 118. http://dx.doi.org/10.1002/2013JD020507.
Bergstrom, R.W., Pilewskie, P., Russell, P.B., Redemann, J., Bond, T.C., Quinn, P.K., Sierau, B., 2007. Spectral absorption properties of atmospheric aerosols. Atmos. Chem. Phys., 7, 5937–5943, (http://www.atmos-chem-phys.net/7/5937/2007).
Bibi, H., Alam, K., Bibi, S., 2016. In-depth discrimination of aerosol types using multiple clustering techniques over four locations in Indo-Gangetic plains. Atmos. Res. 181, 106–114 (http://dx.doi.org/10.1016/j.atmosres.2016.06.017).
Bisht, D.S., Dumka, U.C., Kaskaoutis, D.G., Pipal, A.S., Srivastava, A.K., Soni, V., Attri, S.D., Sateesh, M., Tiwari, S., 2015. Carbonaceous aerosols and pollutants over Delhi urban

environment: temporal evolution, source apportionment and radiative forcing. Sci. Total Environ. 521–522, 431–445 (http://dx.doi.org/10.1016/j.scitotenv.2015.03.083).
Bollasina, M., Nigam, S., Lau, K.-M., 2008. Absorbing aerosols and summer monsoon evolution over South Asia: an observational portrayal. J. Clim. 21, 3221–3239 (http://dx.doi.org/10.1175/2007JCLI2094.1).
Bond, T.C., Doherty, S.J., Fahey, D.W., Forster, P.M., Berntsen, T., DeAngelo, B.J., Flanner, M.G., Ghan, S., Käarcher, B., Koch, D., Kinne, S., Kondo, Y., Quinn, P.K., Sarofim, M.C., Schultz, M.G., Schulz, M., Venkataraman, C., Zhang, H., Zhang, S., Bellouin, N., Guttikunda, S.K., Hopke, P.K., Jacobson, M.Z., Kaiser, J.W., Klimont, Z., Lohmann, U., Schwarz, J.P., Shindell, D., Storelvmo, T., Warren, S.G., Zender, C.S., 2013. Bounding the role of black carbon in the climate system: a scientific assessment. J. Geophys. Res. 118, 5380–5552 (http://dx.doi.org/10.1002/jgrd.50171).
Campanelli, M., Nakajima, T., Olivieri, B., 2004. Determination of the solar calibration constant for a sun-sky radiometer: proposal of an in-situ procedure. Appl. Opt. 43, 651–659.
Campanelli, M., Estellés, V., Tomasi, C., Nakajima, T., Malvestuto, V., Martínez-Lozano, J.A., 2007. Application of the SKYRAD improved Langley plot method for the in situ calibration of CIMEL sun-sky photometers. Appl. Opt. 46, 2688–2702.
Chand, D., Wood, R., Anderson, T.L., Satheesh, S.K., Charlson, R.J., 2009. Satellite-derived direct radiative effect of aerosols dependent on cloud cover. Nat. Geosci. 2, 181–184.
Chin, M., Ginoux, P., Lucchesi, R., Huebert, B., Weber, R., Anderson, T., Masonis, S., Blomquist, B., Bandy, A., Thornton, D., 2003. A global aerosol model forecast for the ACE-Asia field experiment. J. Geophys. Res. 108 (D23), 8654 http://dx.doi.org/10.1029/2003JD003642.
Cui, H., Mao, P., Zhao, Y., Nielsen, C.P., Zhang, J., 2015. Patterns in atmospheric carbonaceous aerosols in China: emission estimates and observed concentrations. Atmos. Chem. Phys. 15, 8657–8678. http://dx.doi.org/10.5194/acp-15-8657-2015.
Das, S.K., Jayaraman, A., 2011. Role of black carbon in aerosol properties and radiative forcing over western India during premonsoon period. Atmos. Res. 102, 320–334.
Das, S.K., Chatterjee, A., Ghosh, S.K., Raha, S., 2015. An integrated campaign for investigation of winter-time continental haze over Indo-Gangetic Basin and its radiative effects. Sci. Total Environ. 533, 370–382.
Derimian, Y., Karnieli, A., Kaufman, Y.J., Andreae, M.O., Andreae, T.W., Dubovik, O., et al, 2008. The role of iron and black carbon in aerosol light absorption. Atmos. Chem. Phys., 8, 3623–37. (http://dx.doi.org/10.5194/acp-8-3623-2008)
Dey, S., Tripathi, S.N., 2008. Aerosol direct radiative effects over Kanpur in the Indo-Gangetic basin, northern India: long-term (2001–2005) observations and implications to regional climate. J. Geophys. Res. 113, D04212 (http://dx.doi.org/10.1029/2007JD009029).
Dey, S., Tripathi, S.N., Singh, R.P., 2004. Influence of dust storms on the aerosol optical properties over the Indo-Gangetic basin. J. Geophys. Res. 109, D20211. http://dx.doi.org/10.1029/2004JD004924.
Draxler, R.R., Rolph, G.D., 2016. HYSPLIT (HYbrid Single-particle Lagrangian Integrated Trajectory) model access via NOAA ARL READY. NOAA Air Resources Laboratory, Silver Spring, MD. Website (http://ready.arl.noaa.gov/HYSPLIT.php).
Dubovik, O., Holben, B.N., Eck, T.F., Smirnov, A., Kaufman, Y.J., King, M.D., Tanre, D., Slutsker, I., 2002. Variability of absorption and optical properties of key aerosol types observed in worldwide locations. J. Atmos. Sci. 59, 590–608.
Dumka, U.C., Moorthy, K.K., Satheesh, S.K., Sagar, R., Pant, P., 2008. Short-period modulations in aerosol optical depths over the central Himalayas: role of mesoscale processes. J. Appl. Meteorol. Clim. 47, 1467–1475. http://dx.doi.org/10.1175/2007JAMC1638.1.
Dumka, U.C., Moorthy, K.K., Kumar, R., Hegde, P., Sagar, R., Pant, P., Singh, N., Babu, S.S., 2010. Characteristics of aerosol black carbon mass concentration over a high altitude location in the Central Himalayas from multi-year measurements. Atmos. Res. 96, 510–521. http://dx.doi.org/10.1016/j.atmosres.2009.12.010.
Dumka, U.C., Manchanda, R.K., Sinha, P.R., Sreenivasan, S., Moorthy, K.K., Babu, S.S., 2013. Temporal variability and radiative impact of black carbon aerosol over tropical urban station Hyderabad. J. Atmos. Solar-Terr. Phys. 105–106, 81–90. http://dx.doi.org/10.1016/j.jastp.2013.08.003.
Dumka, U.C., Tripathi, S.N., Misra, A., Giles, D.M., Eck, T.F., Sagar, R., Holben, B.N., 2014. Latitudinal variation of aerosol properties from Indo-Gangetic Plain to central Himalayan foothills during TIGERZ campaign. J. Geophys. Res. 119. http://dx.doi.org/10.1002/2013JD021040.
Dumka, U.C., Kaskaoutis, D.G., Srivastava, M.K., Devara, P.C.S., 2015. Scattering and absorption properties of near-surface aerosol over Gangetic–Himalayan region: the role of boundary-layer dynamics and long-range transport. Atmos. Chem. Phys. 15, 1555–1572. http://dx.doi.org/10.5194/acp-15-1555-2015.
Eck, T.F., Holben, B.N., Reid, J.S., Dubovik, O., Smirnov, A., O'Neill, N.T., Slutsker, I., Kinne, S., 1999. Wavelength dependence of the optical depth of biomass burning, urban, and desert dust aerosols. J. Geophys. Res. 104 (D24), 31,333–31,349. http://dx.doi.org/10.1029/1999JD900923.
Eck, T.F., Holben, B.N., Dubovik, O., Smirnov, A., Goloub, P., Chen, H.B., et al., 2005. Columnar aerosol optical properties at AERONET sites in central eastern Asia and aerosol transport to the tropical mid-Pacific. J. Geophys. Res. 110 (http://dx.doi.org/10.1029/2004JD005274).
Eck, T.F., et al., 2010. Climatological aspects of the optical properties of fine/coarse mode aerosol mixtures. J. Geophys. Res. 115, D19205. http://dx.doi.org/10.1029/2010JD014002.
Estellés, V., Campanelli, M., Smyth, T.J., Utrillas, M.P., Martínez-Lozano, J.A., 2012. Evaluation of the new ESR network software for the retrieval of direct sun products from CIMEL CE 318 and PREDE POM01 sun-sky radiometers. Atmos. Chem. Phys. 12, 11619–11630. http://dx.doi.org/10.5194/acp-12-11619-2012.
Ganguly, D., Jayaraman, A., 2006. Physical and optical properties of aerosols over an urban location in western India: Implications for shortwave radiative forcing. J. Geophys. Res. 111, D24207. http://dx.doi.org/10.1029/2006JD007393.
Ganguly, D., Jayaraman, A., Rajesh, T.A., Gadhavi, H., 2006a. Wintertime aerosol properties during foggy and nonfoggy days over urban center Delhi and their implications for shortwave radiative forcing. J. Geophys. Res. 111, D15217. http://dx.doi.org/10.1029/2005JD007029.
Ganguly, D., Jayaraman, A., Gadhavi, H., 2006b. Physical and optical properties of aerosols over an urban location in western India: seasonal variabilities. J. Geophys. Res. 111, D24206. http://dx.doi.org/10.1029/2006JD007392.
Gautam, R., Hsu, C.N., Lau, K.-M., 2010. Premonsoon aerosol characterization and radiative effects over the Indo-Gangetic Plains: Implications for regional climate warming. J. Geophys. Res. 115, D17208. http://dx.doi.org/10.1029/2010JD013819.
Giles, D.M., Holben, B.N., Tripathi, S.N., Eck, T.F., et al., 2011. Aerosol properties over the Indo-Gangetic Plain: a mesoscale perspective from the TIGERZ experiment. J. Geophys. Res. 116, D18203. http://dx.doi.org/10.1029/2011JD015809.
Giles, D.M., Holben, B.N., Eck, T.F., Sinyuk, A., Smirnov, A., Slutsker, I., et al., 2012. An analysis of AERONET aerosol absorption properties and classifications representative of aerosol source regions. J. Geophys. Res. 117 (http://dx.doi.org/10.1029/2012JD018127).
Gobbi, G.P., Kaufman, Y.J., Koren, I., Eck, T.F., 2007. Classification of aerosol properties derived from AERONET direct sun data. Atmos. Chem. Phys. 7, 453–458.
Hansen, J., Sato, M., Ruedy, R., Lacis, A., Oinas, V., 2000. Global warming in the twenty-first century: an alternative scenario. Proc. Natl. Acad. Sci. U. S. A. 97, 9875–9880.
IPCC, 2013. Contribution of Working Group I to the Fifth Assessment Report of the Intergovernmental Panel on climate change. In: Stocker, T.F., Qin, D., Plattner, G.-K., Tignor, M., Allen, S.K., Boschung, J., Nauels, A., Xia, Y., Bex, V., Midgley, P.M. (Eds.), Summary for Policymakers in Climate Change 2013: the Physical Science Basis. Cambridge University Press, Cambridge, United Kingdom and New York, NY, USA (27 pp).
Jish Prakash, P., Stenchikov, G., Kalenderski, S., Osipov, S., Bangalath, H., 2014. The impact of dust storms on the Arabian Peninsula and the Red Sea. Atmos. Chem. Phys. Discuss. 14, 19181–19245.
Kar, J., Deeter, M.N., Fishman, J., Liu, Z., Omar, A., Creilson, J.K., Trepte, C.R., Vaughan, M.A., Winker, D.M., 2010. Wintertime pollution over the Eastern Indo-Gangetic Plains as observed from MOPITT, CALIPSO and tropospheric ozone residual data. Atmos. Chem. Phys. 10, 12,273–12,283. http://dx.doi.org/10.5194/acp-10-12273-2010.
Kaskaoutis, D.G., Kambezidis, H.D., Hatzianastassiou, N., Kosmopoulos, P.G., Badarinath, K.V.S., 2007. Aerosol climatology: dependence of the Ångström exponent on wavelength over four AERONET sites. Atmos. Chem. Phys. Discuss. 7, 7347–7397.
Kaskaoutis, D.G., Badarinath, K.V.S., Kharol, S.K., Sharma, A.R., Kambezidis, H.D., 2009. Variations in the aerosol optical properties and types over the tropical urban site of Hyderabad, India. J. Geophys. Res. 114, D22204 (http://dx.doi.org/10.1029/2009JD012423).
Kaskaoutis, D.G., Kalapureddy, M.C.R., Moorthy, K.K., Devara, P.C.S., Nastos, P.T., Kosmopoulos, P.G., Kambezidis, H.D., 2010. Heterogeneity in pre-monsoon aerosol types over the Arabian Sea deduced from shipboard measurements of spectral AODs. Atmos. Chem. Phys. 10, 4893–4908.
Kaskaoutis, D.G., Kharol, S.K., Sinha, P.R., Singh, R.P., Badarinath, K.V.S., Mehdi, W., Sharma, M., 2011a. Contrasting aerosol trends over South Asia during the last decade based on MODIS observations. Atmos. Measur. Techn. Discuss. 4, 5275–5323.
Kaskaoutis, D.G., Kharol, S.K., Sinha, P.R., Singh, R.P., Kambezidis, H.D., Sharma, A.R., Badarinath, K.V.S., 2011b. Extremely large anthropogenic-aerosol contribution to total aerosol load over the Bay of Bengal during winter season. Atmos. Chem. Phys. 11, 7097–7117.
Kaskaoutis, D.G., Gautam, R., Singh, R.P., Houssos, E.E., Goto, D., Singh, S., Bartzokas, A., Kosmopoulos, P.G., Sharma, M., Hsu, N.C., Holben, B.N., Takemura, T., 2012. Influence of anomalous dry conditions on aerosols over India: transport, distribution and properties. J. Geophys. Res. 117, D09106. http://dx.doi.org/10.1029/2011JD017314.
Kaskaoutis, D.G., Sinha, P.R., Vinoj, V., Kosmopoulos, P.G., Tripathi, S.N., Misra, A., Sharma, M., Singh, R.P., 2013. Aerosol properties and radiative forcing over Kanpur during severe aerosol loading conditions. Atmos. Environ. 79, 7–19.
Kaskaoutis, D.G., Kumar, S., Sharma, D., Singh, R.P., Kharol, S.K., Sharma, M., Singh, A.K., Singh, S., Singh, A., Singh, D., 2014. Effects of crop residue burning on aerosol properties, plume characteristics and long-range transport over northern India. J. Geophys. Res. 119, 5424–5444. http://dx.doi.org/10.1002/2013JD021357.
Kedia, S., Ramachandran, S., Holben, B.N., Tripathi, S.N., 2014. Quantification of aerosol type, and source of aerosols over the Indo-Gangetic plain. Atmos. Environ. 98, 607–619.
Kobayashi, E., Uchiyama, A., Yamazaki, A., Kudo, R., 2010. Retrieval of aerosol optical properties based on the spheroid model. J. Meteorol. Soc. Japan. 88, 847–856.
Kumar, K.R., Sivakumar, V., Reddy, R.R., Gopal, K.R., Adesina, A.J., 2013. Inferring wavelength dependence of AOD and Angstrom exponent over a sub-tropical station in South Africa using AERONET data: influence of meteorology, long-range transport and curvature effect. Sci. Total Environ. 461–462, 397–408.
Kumar, K.R., Sivakumar, V., Reddy, R.R., Gopal, K.R., Adesina, A.J., 2014. Identification and classification of different aerosol types over a subtropical rural site in Mpumalanga, South Africa: Seasonal variations as retrieved from the AERONET Sun photometer. Aerosol. Air Qual. Res. 14, 108–123.
Kumar, S., Kumar, S., Kaskaoutis, D.G., Singh, R.P., Singh, R.K., Mishra, A.K., Srivastava, M.K., Singh, A.K., 2015a. Meteorological, atmospheric and climatic perturbations during major dust storms over Indo-Gangetic basin. Aeol. Res. 17, 15–31.
Kumar, K.R., Yin, Y., Sivakumar, V., Kang, N., Yu, X., Diao, Y., Adesina, A.J., Reddy, R.R., 2015b. Aerosol climatology and discrimination of aerosol types retrieved from MODIS, MISR, and OMI over Durban (29.88°S, 31.02°E), South Africa. Atmos. Environ. 117, 9–18.
Lawrence, M.G., 2011. Atmospheric science: Asia under a high-level brown cloud. Nat. Geosci. 4 (30), 352–353.
Lawrence, M.G., Lelieveld, J., 2010. Atmospheric pollutant outflow from Southern Asia: a review. Atmos. Chem. Phys. 10, 11017–11096. http://dx.doi.org/10.5194/acp-10-11017-2010.
Liou, K.N., 2002. An Introduction to Atmospheric Radiation. 2nd edition. International Geophysics Series 84. Academic Press, San Diego (583 pp.).

Lu, Z., Streets, D.G., Zhang, Q., Wang, S., Carmichael, G.R., Cheng, Y.F., Wei, C., Chin, M., Diehl, T., Tan, Q., 2010. Sulfur dioxide emissions in China and sulfur trends in East Asia since 2000. Atmos. Chem. Phys. 10, 6311–6331. http://dx.doi.org/10.5194/acp-10-6311-2010.

Moorthy, K.K., Babu, S.S., Satheesh, S.K., Srinivasan, J., Dutt, C.B.S., 2007. Dust absorption over the "Great Indian Desert" using ground-based and satellite remote sensing. J. Geophys. Res. 112, D09206. http://dx.doi.org/10.1029/2006JD007690.

Moorthy, K.K., Babu, S.S., Manoj, M.R., Satheesh, S.K., 2013. Build-up of aerosols over the Indian Region. Geophys. Res. Lett. 40, 1011–1014. http://dx.doi.org/10.1002/grl.50165.

Nakajima, T., Hayasaka, T., Higurashi, A., Hashida, G., Moharram-Nejad, N., Najafi, Y., Valavi, H., 1996a. Aerosol optical properties in the Iranian Region obtained by ground based solar measurements in the summer of 1991. J. Appl. Meteorol. 35, 1265–1278.

Nakajima, T., Tonna, G., Rao, R., Boi, P., Kaufman, Y., Holben, B., 1996b. Use of sky brightness measurements from ground for remote sensing of particulate polydispersions. Appl. Opt. 15, 2672–2686.

O'Neill, N.T., Ignatov, A., Holben, B.N., Eck, T.F., 2000. The lognormal distribution as a reference for reporting aerosol optical depth statistics; empirical tests using multi-year, multi-site AERONET sun photometer data. Geophys. Res. Lett. 27, 3333–3336.

Pace, G., di Sarra, A., Meloni, D., Piacentino, S., Chamard, P., 2006. Aerosol optical properties at Lampedusa (central Mediterranean). 1. Influence of transport and identification of different aerosol types. Atmos. Chem. Phys. 6, 697–713.

Pandithurai, G., Dipu, S., Dani, K.K., Tiwari, S., Bisht, D.S., Devara, P.C.S., Pinker, R.T., 2008. Aerosol radiative forcing during dust events over New Delhi, India. J. Geophys. Res. 113, D13209. http://dx.doi.org/10.1029/2008JD009804.

Pathak, B., Pradip, K.B., Gogoi, M.M., Bhuyan, K., 2012. Seasonal heterogeneity in aerosol types over Dibrugarh-North-Eastern India. Atmos. Environ. 47, 307–315. http://dx.doi.org/10.1016/j.atmosenv.2011.10.061.

Prasad, A.K., Singh, R.P., 2007. Changes in aerosol parameters during major dust storm events (2001–2005) over the Indo-Gangetic Plains using AERONET and MODIS data. J. Geophys. Res. 112, D09208. http://dx.doi.org/10.1029/2006JD007778.

Prasad, A.K., Singh, S., Chauhan, S.S., Srivastava, M.K., Singh, R.P., Singh, R., 2007. Aerosol radiative forcing over the Indo-Gangetic plains during major dust storms. Atmos. Environ. 41, 6289–6301.

Ram, K., Sarin, M.M., Tripathi, S.N., 2010. A 1-year record of carbonaceous aerosols from an urban site in the Indo-Gangetic Plain: characterization, sources, and temporal variability. J. Geophys. Res. 115, D24313. http://dx.doi.org/10.1029/2010JD014188.

Ramachandran, S., Kedia, S., 2010. Black carbon aerosols over an urban region: radiative forcing and climate impact. J. Geophys. Res. 115, D10202. http://dx.doi.org/10.1029/2009JD013560.

Raman, R.S., Ramachandran, S., 2010. Annual and seasonal variability of ambient aerosols over an urban region in western India. Atmos. Environ. 44, 1200–1208.

Ramanathan, V., Crutzen, P.J., Kiehl, J.T., Rosenfeld, D., 2001. Aerosols, climate, and the hydrologic cycle. Science 294, 2119–2124.

Rashki, A., Kaskaoutis, D.G., Francois, P., Kosmopoulos, P.G., Legrand, M., 2015. Dust-storm dynamics over Sistan region, Iran: seasonality, transport characteristics and affected areas. Aeol. Res. 16, 35–48.

Ricchiazzi, P., Yang, S., Gautier, C., Sowle, D., 1998. SBDART: A research and teaching software tool for plane-parallel radiative transfer in the Earth's atmosphere. Bull. Am. Meteorol. Soc. 79 (2101–2014).

Russell, P.B., Bergstorm, R.W., Shinozuka, Y., Clarke, A.D., De Carlo, P.F., Jimenez, J.L., Livingston, J.M., Redemann, J., et al., 2010. Absorption Ångström exponent in AERONET and related data as an indicator of aerosol composition. Atmos. Chem. Phys. 10, 1155–1169.

Saikawa, E., Kurokawa, J., Takigawa, M., Borken-Kleefeld, J., Mauzerall, D.L., Horowitz, L.W., Ohara, T., 2011. The impact of China's vehicle emissions on regional air quality in 2000 and 2020: a scenario analysis. Atmos. Chem. Phys. 11, 9465–9484. http://dx.doi.org/10.5194/acp-11-9465-2011.

Satheesh, S.K., Moorthy, K.K., 2005. Radiative effects of natural aerosols: a review. Atmos. Environ. 39, 2089–2110. http://dx.doi.org/10.1016/j.atmosenv.2004.12.029.

Satheesh, S.K., Ramanathan, V., 2000. Large differences in tropical aerosol forcing at the top of the atmosphere and Earth's surface. Nature 405, 60–63.

Schuster, G.L., Dubovik, O., Holben, B.N., 2006. Angstrom exponent and bimodal aerosol size distributions. J. Geophys. Res. 111 (http://dx.doi. org/10.1029/2005JD006328).

Sharma, D., Singh, D., Kaskaoutis, D.G., 2012. Impact of two intense dust storms on aerosol characteristics and radiative forcing over Patiala, in the North-West India. Adv. Meteorol., ID 956814, doi:http://dx.doi.org/10.1155/2012/956814.

Shukla, A.K., Babu, K.N., Prajapati, R.P., Suthar, N.M., Ajai, Sinha, A., Saifee, A.M., Satashia, S.N., Arul Muthiah, M., Venkatesan, R., 2013. An ocean CAL-VAL site at Kavaratti in Lakshadweep for vicarious calibration of OCM-2 and validation of geo-physical products - development & operationalization. Mar. Geod. 36, 203–218.

Singh, R.P., Dey, S., Tripathi, S.N., Tare, V., Holben, B., 2004. Variability of aerosol parameters over Kanpur, northern India. J. Geophys. Res. 109, D23206. http://dx.doi.org/10.1029/2004JD004966.

Sinha, P.R., Kaskaoutis, D.G., Manchanda, R.K., Sreenivasan, S., 2012. Characteristics of aerosols over Hyderabad in southern Peninsular India: synergy in the classification techniques. Ann. Geophys. 30, 1393–1410. http://dx.doi.org/10.5194/angeo-30-1393-2012.

Sinha, P.R., Dumka, U.C., Manchanda, R.K., Kaskaoutis, D.G., Sreenivasan, S., Moorthy, K.K., Babu, S.S., 2013. Contrasting aerosol characteristics and radiative forcing over Hyderabad, India due to seasonal mesoscale and synoptic-scale processes. Q. J. R. Meteorol. Soc. 139, 434–450. http://dx.doi.org/10.1002/qj.1963.

Srivastava, R., Ramachandran, S., 2013. The mixing state of aerosols over the Indo-Gangetic Plain and its impact on radiative forcing. Q. J. R. Meteorol. Soc. 139, 137–151.

Srivastava, A.K., Tripathi, S.N., Dey, S., Kanawade, V.P., Tiwari, S., 2012. Inferring aerosol types over the Indo-Gangetic Basin from ground based sun photometer measurements. Atmos. Res. 109-110, 64–75. http://dx.doi.org/10.1016/j.atmosres.2012.02.010.

Srivastava, A.K., Soni, V.K., Singh, S., Kanawade, V.P., Singh, N., Tiwari, S., Attri, S.D., 2014a. An early South Asian dust storm during March 2012 and its impacts on Indian Himalayan foothills: a case study. Sci. Total Environ. 493, 526–534.

Srivastava, A.K., Yadav, V., Pathak, V., Singh, S., Tiwari, S., Bisht, D.S., Goloub, P., 2014b. Variability in radiative properties of major aerosol types: a year-long study over Delhi—an urban station in Indo-Gangetic Basin. Sci. Total Environ. 473–474, 659–666 (http://dx.doi.org/10.1016/j.scitotenv.2013.12.064).

Vijayakumar, K., Devara, P.C.S., 2013. Study of aerosol optical depth, ozone, and precipitable water vapour content over Sinhagad, a high-altitude station in the Western Ghats. Int. J. Remote Sens. 34, 613–630.

Wang, L., Zhou, X., Ma, Y., Cao, Z., Wu, R., Wang, W., 2016. Carbonaceous aerosols over China—review of observations, emissions, and climate forcing. Environ. Sci. Pollut. Res. 23, 1671–1680. http://dx.doi.org/10.1007/s11356-015-5398-2.

Wu, Y., Zhu, J., Che, H., Xia, X., Zhang, R., 2015. Column-integrated aerosol optical properties and direct radiative forcing based on sun photometer measurements at a semi-arid rural site in northeast China. Atmos. Res. 157, 56–65.

Yoon, J., von Hoyningen-Huene, W., Vountas, M., Burrows, J.P., 2011. Analysis of linear long-term trend of aerosol optical thickness derived from SeaWiFS using BAER over Europe and South China. Atmos. Chem. Phys. 11, 12149–12167. http://dx.doi.org/10.5194/acp-11-12149-2011.

Yoon, J., Von Hoyningen-Huene, W., Kokhanovsky, A.A., Vountas, M., Burrows, J.P., 2012. Trend analysis of aerosol optical thickness and Ångström exponent derived from the global AERONET spectral observations. Atmos. Meas. Tech. 5, 1271–1299. http://dx.doi.org/10.5194/amt-5-1271-2012.

Yoon, J., Burrows, J.P., Vountas, M., Von Hoyningen-Huene, W., Chang, D.Y., Richter, A., Hilboll, A., 2014. Changes in atmospheric aerosol loading retrieved from space-based measurements during the past decade. Atmos. Chem. Phys. 14, 6881–6902.

Yu, X., Kumar, K.R., Lü, R., Ma, J., 2016. Changes in column aerosol optical properties during extreme haze-fog episodes in January 2013 over urban Beijing. Environ. Pollut. 210, 217–226.